AIAA 91-0770
Stabilization of the Burnett Equations and Application to High-Altitude Hypersonic Flows

X. Zhong
R. W. MacCormack
D. R. Chapman
Stanford Univ., Stanford, CA

29th Aerospace Sciences Meeting
January 7–10, 1991/Reno, Nevada

AIAA-91-0770

STABILIZATION OF THE BURNETT EQUATIONS AND APPLICATION TO HIGH-ALTITUDE HYPERSONIC FLOWS

Xiaolin Zhong *
Robert W. MacCormack †
Dean R. Chapman ‡
Department of Aeronautics and Astronautics
Stanford University, Stanford, CA 94305

Abstract

It is shown from both analytical investigation and numerical computations that the 1D and plane-2D Burnett equations are unstable to disturbances of small wavelengths. This fundamental instability arises in numerical computations when the grid spacing is less than the order of a mean free path, and precludes Burnett flow-field computations above a certain maximum altitude for any given vehicle . A new set of equations termed the "augmented Burnett equations" has been developed, and shown to be stable both by a linearized stability analysis and by direct numerical computations for 1D and 2D flows. The latter represent the first known Burnett solutions for 2D hypersonic flow over a blunt leading edge. Comparison of these solutions with the conventional Navier-Stokes solutions reveals that the difference to be small at low altitudes, but significant at high altitudes. Burnett CFD appears to be especially important for predicting aerodynamic parameters sensitive to flow-field details, such as radiation, at high attitudes.

1. Introduction

A number of advanced hypersonic vehicles are anticipated to operate in the continuum transitional regime at high altitudes where the thickness of the bow shock waves is a sizable or dominant part of the shock detachment distance. Under these conditions, CFD codes for the flow past the vehicles must compute through the structure of hypersonic shock waves. However, it has long been known that the conventional Navier-Stokes equations are inaccurate for this purpose, and hence we need to develop some other set of constitutive equations, more advanced than Navier-Stokes, to provide realistic continuum-flow computations for hypersonic flows at these high altitudes.

The development of an advanced set of continuum equations of motion is necessary for certain practical applications. Aeroassisted vehicles such as the AOTV and the AFE operate mainly at altitudes in the continuum transitional regime. Anticipated applications here would be to their aerodynamic stability and heating parameters as well as to flow-field radiation. A similar situation exists for some Mars return vehicles that would use high-altitude aerobraking to change orbit. Still other applications involve certain aerothermodynamic computations for the upper portion of the ascent trajectory of vehicles such as the NASP which have cowl lips and leading edges with relatively small radius of curvature. These are subjected to very severe heating rates in the continuum transitional regime where the numerical computations using the Navier-Stokes equations are inaccurate. Additional relevant applications are to hypersonic flow-field radiation at high altitudes, which can be important both to the heating rate on vehicles such as the AOTV, as well as to the hard-body radiation signature of a missile traveling through the upper atmosphere.

It is noted that a completely different approach to that investigated herein for circumventing the inaccuracy of Navier-Stokes CFD is to use particulate-flow computations such as the DSMC method of Bird[1] and the particle simulation method of Baganoff[2, 3]. This type of flow simulation, however, can require relatively large amount of computer time, especially at lower altitudes. Hence the development of an advanced set of continuum equations having a reasonable accuracy should be much more computationally efficient.

In order to develop the advanced set of constitutive equations, Fiscko and Chapman[4, 5] reinvestigated and proposed the Burnett equations[6], which are higher order approximations to the Boltzmann equation than the Navier-Stokes equations. They found that the Burnett equations provide much greater accuracy than the Navier-Stokes equations for one-dimensional shock wave structure in monatomic gases. However, both an analytical analysis[7] and the past computational experience[8] showed that the Burnett equations are unstable to very small wavelength disturbances encountered in fine-mesh numerical solutions. This unstability makes it impossible to apply the Burnett equa-

*Graduate Student
†Professor, Member AIAA
‡Professor, Fellow AIAA

tions to practical flows in two and three dimensions above a certain altitude for any vehicle. Therefore, we need to overcome the instability of the Burnett equations in order to apply the equations to practical flow problems.

Guided by the linearized stability analysis, this paper will develop a new set of equations termed the " augmented Burnett equations" to stablize the conventional Burnett equations. We will show that the augmented Burnett equations are stable and yield essentially the same results as the conventional Burnett equations when stable solutions exist for the later equations. The new set of equations has been tested by a theoretical stability analysis as well as 1D and 2D flow computations following the objectives below.

The Research Objectives

1. To develop augmented Burnett equations which overcome the instabilities encountered when fine-mesh computations are attempted with the conventional Burnett equations.

2. To test the computational stability of both the conventional Burnett equations and the augmented Burnett equations by solving them numerically with progressively refined meshes for both one-dimensional hypersonic shock structure, and two-dimensional flows past a blunt leading edge.

3. To test the accuracy of the augmented Burnett equations by comparing their results with the existing experimental data and the DSMC results on hypersonic shock structure in argon.

4. To compare the two-dimensional Burnett flow field with the corresponding Navier-Stokes flow field using the same set of surface boundary conditions; Also to compare the computational results of the two equations with existing experimental data and DSMC results. The two test cases computed are:

   - Supersonic and hypersonic flows past cylindrical blunt leading edges at both low and high altitudes;
   - Hypersonic flows with rotational nonequilibrium past a double-ellipse-shaped blunt body.

2. The Governing Equations

We first consider the one-dimensional governing equations for stability analysis and for shock wave structure computations. The mass, momentum and energy conservation equations for a compressible viscous flow without rotational, vibrational and chemical nonequilibrium are as follows:

$$\frac{\partial U}{\partial t} + \frac{\partial F}{\partial x} = 0 \tag{1}$$

where

$$U = \left\{ \begin{array}{c} \rho \\ \rho u \\ e \end{array} \right\},$$

$$F = \left\{ \begin{array}{c} \rho u \\ \rho u^2 + p + \sigma_{11} \\ (e + p + \sigma_{11})\, u + q_1 \end{array} \right\},$$

$$p = \rho R T,$$

$$e = \rho \left(c_v T + \frac{u^2}{2} \right)$$

and σ_{11} and q_1 are the viscous stress and the heat flux terms, of which the relations with the gradients of the flow variables are termed the constitutive equations.

Eq. (1) together with the two constitutive equations for σ_{11} and q_1 given in the next section form a complete set of governing equations for the one-dimensional gas flow.

3. The Constitutive Equations

The gas flow regime can be characterized by the Kundsen number Kn, which is defined as:

$$Kn = \frac{\lambda}{L} \tag{2}$$

where λ is the mean free path and L is the macroscopic characteristic length of the flow. When Kn increases from 0 through the order of 1 to ∞, the gas flow changes from the translational equilibrium regime through the transitional regime to the free molecule regime.

The constitutive equations for a gas flow of small Kn can be derived as approximate solutions of the Boltzmann equation, which is accepted as the general governing equations for gas at any Kn. The Boltzman equation is solved by a successive iteration method, i.e. the Chapman-Enskog method[6], which leads to the following general three-dimensional constitutive equations:

$$\left\{ \begin{array}{rcl} \sigma_{ij} & = & \sigma_{ij}^{(0)} + \sigma_{ij}^{(1)} + \sigma_{ij}^{(2)} + \sigma_{ij}^{(3)} + \cdots \\ q_i & = & q_i^{(0)} + q_i^{(1)} + q_i^{(2)} + q_i^{(3)} + \cdots \end{array} \right. \tag{3}$$

where $i = 1, 2, 3$ and $j = 1, 2, 3$ and the superscript numbers represent the order of accuracy of the solutions.

When $Kn \approx 0$, only the first terms in the equations are needed and we obtain the zero-order Euler equations, i.e.,

$$\sigma_{ij}^{(0)} = 0 \tag{4}$$

and

$$q_i^{(0)} = 0\,. \tag{5}$$

As Kn increases, the flow departs from the equilibrium regime. Hence more and more high order terms in Eq. (3) become significant and are needed to solve the flow equations accurately.

When the gas flow departs slightly from equilibrium ($Kn < 0.1$), we only need to retain the first two terms and obtain the first-order Navier-Stokes equations, which contain the first-order derivatives of the flow variables in the constitutive equations; As Kn becomes larger, we need to retain the first three terms and obtain the second-order Burnett equations, which contain the second derivatives and the products of the first derivatives; Similarly, the third-order solutions are the super Burnett equations; and so on.

Therefore, the constitutive equations of the nth order approximation are:

$$\begin{cases} \sigma_{ij} \approx \sigma_{ij}^{(1)} + + \cdots + \sigma_{ij}^{(n)} \\ q_i \approx q_i^{(1)} + + \cdots + q_i^{(n)} \end{cases} \tag{6}$$

where n represents the level of approximations, i.e.,

$$\begin{cases} n=1 & \text{the Navier-Stokes equations} \\ n=2 & \text{the Burnett equations} \\ n=3 & \text{the super Burnett equations} \\ & \vdots \end{cases}$$

The detailed expressions for $\sigma_{ij}^{(n)}$ and $q_i^{(n)}$ are given as follows ($n = 1, 2, 3$) :

The First-order Solutions

The general expressions for $\sigma_{ij}^{(1)}$ and $q_i^{(1)}$ are:

$$\sigma_{ij}^{(1)} = -2\mu \overline{\frac{\partial u_i}{\partial x_j}}, \tag{7}$$

$$q_i^{(1)} = -\kappa \frac{\partial T}{\partial x_i} \tag{8}$$

where a bar over a derivative designates a nondivergent symmetrical tensor, i.e.,

$$\overline{A_{ij}} = \begin{cases} \frac{A_{ij}+A_{ji}}{2} - \frac{1}{3} A_{kk} & \text{if } i = j \\ \frac{A_{ij}+A_{ji}}{2} & \text{if } i \neq j \end{cases}$$

and

$$A_{kk} = A_{11} + A_{22} + A_{33} .$$

In one dimension, the general expressions reduce to

$$\sigma_{11}^{(1)} = -\frac{4}{3}\mu u_x , \tag{9}$$

$$q_1^{(1)} = -\kappa T_x . \tag{10}$$

In two dimensions, the general expressions reduce to

$$\sigma_{11}^{(1)} = \frac{2}{3}\mu (u_x + v_y) - 2\mu u_x , \tag{11}$$

$$\sigma_{12}^{(1)} = \sigma_{21}^{(1)} = -\mu (u_y + v_x) , \tag{12}$$

$$\sigma_{22}^{(1)} = \frac{2}{3}\mu (u_x + v_y) - 2\mu v_y \tag{13}$$

and

$$q_1^{(1)} = -\kappa T_x , \tag{14}$$

$$q_2^{(1)} = -\kappa T_y \tag{15}$$

where $(\ )_x = \frac{\partial}{\partial x}$ and $(\ )_y = \frac{\partial}{\partial y}$.

The Second-order Solutions

The general expressions for $\sigma_{ij}^{(2)}$ and $q_i^{(2)}$ are[6, 9]:

$$\begin{aligned} \sigma_{ij}^{(2)} = \frac{\mu^2}{p} \Bigg\{ & \omega_1 \frac{\partial u_k}{\partial x_k} \overline{\frac{\partial u_i}{\partial x_j}} \\ & + \omega_2 \Big[-\overline{\frac{\partial}{\partial x_i}\Big(\frac{1}{\rho}\frac{\partial p}{\partial x_j}\Big)} - \overline{\frac{\partial u_k}{\partial x_i}\frac{\partial u_j}{\partial x_k}} - 2\overline{\frac{\partial u_i}{\partial x_k}\frac{\partial u_k}{\partial x_j}} \Big] \\ & + \omega_3 R \overline{\frac{\partial^2 T}{\partial x_i \partial x_j}} + \omega_4 \frac{1}{\rho T} \overline{\frac{\partial p}{\partial x_i}\frac{\partial T}{\partial x_j}} \\ & + \omega_5 \frac{R}{T} \overline{\frac{\partial T}{\partial x_i}\frac{\partial T}{\partial x_j}} + \omega_6 \overline{\frac{\partial u_i}{\partial x_k}\frac{\partial u_k}{\partial x_j}} \Bigg\} \end{aligned} \tag{16}$$

and

$$\begin{aligned} q_i^{(2)} = \frac{\mu^2}{\rho} \Bigg\{ & \theta_1 \frac{1}{T}\frac{\partial u_k}{\partial x_k}\frac{\partial T}{\partial x_i} \\ & + \theta_2 \frac{1}{T}\Big[\frac{2}{3}\frac{\partial}{\partial x_i}\Big(T\frac{\partial u_k}{\partial x_k}\Big) + 2\frac{\partial u_k}{\partial x_i}\frac{\partial T}{\partial x_k}\Big] \\ & + \theta_3 \frac{1}{\rho}\frac{\partial p}{\partial x_k}\overline{\frac{\partial u_k}{\partial x_i}} + \theta_4 \frac{\partial}{\partial x_k}\Big(\overline{\frac{\partial u_k}{\partial x_i}}\Big) \\ & + \theta_5 \frac{1}{T}\frac{\partial T}{\partial x_k}\overline{\frac{\partial u_k}{\partial x_i}} \Bigg\} \end{aligned} \tag{17}$$

where the numerical constants ω_i and θ_i are computed by the Chapman-Enskog method, depending on the gas molecular repulsive force models[9] used. So far, only the coefficients for two extreme cases, the hard-sphere model and the Maxwellian model ($F \propto r^{-5}$), are computed as follows:

	Maxwell Molecules	Hard-Sphere Molecules
ω_1	10/3	4.056
ω_2	2	2.028
ω_3	3	2.418
ω_4	0	0.681
ω_5	3	0.219
ω_6	8	7.424
θ_1	75/8	11.644
θ_2	-45/8	-5.822
θ_3	-3	-3.090
θ_4	3	2.418
θ_5	117/4	25.157

Since the molecular model for a real gas falls in between the two extreme cases above, Lumpkin[10] following Woods[11, 12] used values of ω_i and θ_i for real gases interpolated linearly in the temperature-viscosity exponent (ω) from the data above.

In one dimension, (16) and Eq. (17) reduce to

$$\sigma_{11}^{(2)} = \frac{\mu^2}{p} \left(\alpha_1 u_x^2 + \alpha_7 RT_{xx} + \alpha_9 \frac{RT}{\rho} \rho_{xx} + \alpha_{11} \frac{RT}{\rho^2} \rho_x^2 + \alpha_{12} \frac{R}{\rho} T_x \rho_x + \alpha_{13} \frac{R}{T} T_x^2 \right) \tag{18}$$

and

$$q_1^{(2)} = \frac{\mu^2}{\rho} \left(\gamma_1 \frac{1}{T} T_x u_x + \gamma_3 u_{xx} + \gamma_8 \frac{1}{\rho} \rho_x u_x \right). \tag{19}$$

In two dimensions, the general expressions reduce to

$$\begin{aligned} \sigma_{11}^{(2)} = \frac{\mu^2}{p} \Big(& \alpha_1 u_x^2 + \alpha_2 u_x v_y + \alpha_3 v_y^2 \\ & + \alpha_4 u_y v_x + \alpha_5 u_y^2 + \alpha_6 v_x^2 \\ & + \alpha_7 RT_{xx} + \alpha_8 RT_{yy} + \alpha_9 \frac{RT}{\rho} \rho_{xx} \\ & + \alpha_{10} \frac{RT}{\rho} \rho_{yy} + \alpha_{11} \frac{RT}{\rho^2} \rho_x^2 \\ & + \alpha_{12} \frac{R}{\rho} T_x \rho_x + \alpha_{13} \frac{R}{T} T_x^2 \\ & + \alpha_{14} \frac{RT}{\rho^2} \rho_y^2 + \alpha_{15} \frac{R}{\rho} T_y \rho_y \\ & + \alpha_{16} \frac{R}{T} T_y^2 \Big), \end{aligned} \tag{20}$$

$$\begin{aligned} \sigma_{22}^{(2)} = \frac{\mu^2}{p} \Big(& \alpha_1 v_y^2 + \alpha_2 v_y u_x + \alpha_3 u_x^2 \\ & + \alpha_4 v_x u_y + \alpha_5 v_x^2 + \alpha_6 u_y^2 \\ & + \alpha_7 RT_{yy} + \alpha_8 RT_{xx} + \alpha_9 \frac{RT}{\rho} \rho_{yy} \\ & + \alpha_{10} \frac{RT}{\rho} \rho_{xx} + \alpha_{11} \frac{RT}{\rho^2} \rho_y^2 \\ & + \alpha_{12} \frac{R}{\rho} T_y \rho_y + \alpha_{13} \frac{R}{T} T_y^2 \\ & + \alpha_{14} \frac{RT}{\rho^2} \rho_x^2 + \alpha_{15} \frac{R}{\rho} T_x \rho_x \\ & + \alpha_{16} \frac{R}{T} T_x^2 \Big), \end{aligned} \tag{21}$$

$$\begin{aligned} \sigma_{12}^{(2)} &= \sigma_{21}^{(2)} \\ &= \frac{\mu^2}{p} \Big(\beta_1 u_x u_y + \beta_2 u_y v_y + \beta_2 u_x v_x \\ &\quad + \beta_1 v_x v_y + \beta_3 RT_{xy} + \beta_4 \frac{RT}{\rho} \rho_{xy} \\ &\quad + \beta_5 \frac{R}{T} T_x T_y + \beta_6 \frac{RT}{\rho^2} \rho_x \rho_y \\ &\quad + \beta_7 \frac{R}{\rho} \rho_x T_y + \beta_7 \frac{R}{\rho} \rho_y T_x \Big) \end{aligned} \tag{22}$$

and

$$\begin{aligned} q_1^{(2)} = \frac{\mu^2}{\rho} \Big(& \gamma_1 \frac{1}{T} T_x u_x + \gamma_2 \frac{1}{T} T_x v_y + \gamma_3 u_{xx} \\ & + \gamma_4 u_{yy} + \gamma_5 v_{xy} + \gamma_6 \frac{1}{T} T_y v_x \\ & + \gamma_7 \frac{1}{T} T_y u_y + \gamma_8 \frac{1}{\rho} \rho_x u_x + \gamma_9 \frac{1}{\rho} \rho_x v_y \\ & + \gamma_{10} \frac{1}{\rho} \rho_y u_y + \gamma_{11} \frac{1}{\rho} \rho_y v_x \Big), \end{aligned} \tag{23}$$

$$\begin{aligned} q_2^{(2)} = \frac{\mu^2}{\rho} \Big(& \gamma_1 \frac{1}{T} T_y v_y + \gamma_2 \frac{1}{T} T_y u_x + \gamma_3 v_{yy} \\ & + \gamma_4 v_{xx} + \gamma_5 u_{xy} + \gamma_6 \frac{1}{T} T_x u_y \\ & + \gamma_7 \frac{1}{T} T_x v_x + \gamma_8 \frac{1}{\rho} \rho_y v_y + \gamma_9 \frac{1}{\rho} \rho_y u_x \\ & + \gamma_{10} \frac{1}{\rho} \rho_x v_x + \gamma_{11} \frac{1}{\rho} \rho_x u_y \Big) \end{aligned} \tag{24}$$

where the coefficients α_i's, β_i's and γ_i's are as follows:

$$\begin{cases} \alpha_1 = \frac{2}{3}\omega_1 - \frac{14}{9}\omega_2 + \frac{2}{9}\omega_6 \\ \alpha_2 = \frac{1}{3}\omega_1 + \frac{2}{9}\omega_2 - \frac{2}{9}\omega_6 \\ \alpha_3 = -\frac{1}{3}\omega_1 + \frac{7}{9}\omega_2 - \frac{1}{9}\omega_6 \\ \alpha_4 = -\frac{2}{3}\omega_2 + \frac{1}{6}\omega_6 \\ \alpha_5 = \frac{1}{3}\omega_2 + \frac{1}{12}\omega_6 \\ \alpha_6 = -\frac{2}{3}\omega_2 + \frac{1}{12}\omega_6 \\ \alpha_7 = -\frac{2}{3}\omega_2 + \frac{2}{3}\omega_3 \\ \alpha_8 = \frac{1}{3}\omega_2 - \frac{1}{3}\omega_3 \\ \alpha_9 = -\frac{2}{3}\omega_2 \\ \alpha_{10} = \frac{1}{3}\omega_2 \\ \alpha_{11} = \frac{2}{3}\omega_2 \\ \alpha_{12} = -\frac{2}{3}\omega_2 + \frac{2}{3}\omega_4 \\ \alpha_{13} = \frac{2}{3}\omega_4 + \frac{2}{3}\omega_5 \\ \alpha_{14} = -\frac{1}{3}\omega_2 \\ \alpha_{15} = \frac{1}{3}\omega_2 - \frac{1}{3}\omega_4 \\ \alpha_{16} = -\frac{1}{3}\omega_4 - \frac{1}{3}\omega_5 \end{cases}$$

$$\begin{cases} \beta_1 = \frac{1}{2}\omega_1 - \frac{5}{3}\omega_2 + \frac{1}{6}\omega_6 \\ \beta_2 = \frac{1}{2}\omega_1 - \frac{2}{3}\omega_2 + \frac{1}{6}\omega_6 \\ \beta_3 = -\omega_2 + \omega_3 \\ \beta_4 = -\omega_2 \\ \beta_5 = \omega_4 + \omega_5 \\ \beta_6 = \omega_2 \\ \beta_7 = -\frac{1}{2}\omega_2 + \frac{1}{2}\omega_4 \end{cases}$$

$$\begin{cases} \gamma_1 &= \theta 1 + \frac{8}{3}\theta 2 + \frac{2}{3}\theta 3 + \frac{2}{3}\theta 5 \\ \gamma_2 &= \theta 1 - \frac{1}{3}\theta 3 - \frac{1}{3}\theta 5 + \frac{2}{3}\theta 2 \\ \gamma_3 &= \frac{2}{3}\theta 2 + \frac{2}{3}\theta 4 \\ \gamma_4 &= \frac{1}{2}\theta 4 \\ \gamma_5 &= \frac{1}{6}\theta 4 + \frac{2}{3}\theta 2 \\ \gamma_6 &= 2\theta 2 + \frac{1}{2}\theta 5 + \frac{1}{2}\theta 3 \\ \gamma_7 &= \frac{1}{2}\theta 3 + \frac{1}{2}\theta 5 \\ \gamma_8 &= \frac{2}{3}\theta 3 \\ \gamma_9 &= -\frac{1}{3}\theta 3 \\ \gamma_{10} &= \frac{1}{2}\theta 3 \\ \gamma_{11} &= \frac{1}{2}\theta 3 \end{cases}$$

It is noted that the Chapman-Enskog series expansion, which is generally regarded as only asymptotically convergent, is not the only means of deriving the Burnett equations. Woods[11, 12] has shown that these equations can be derived by two other independent means without reference to this expansion. Thus the uncertain convergence properties of the expansion are not germane to the present investigation.

The Third-order Solutions

The one-dimensional expressions for $\sigma_{ij}^{(3)}$ and $q_i^{(3)}$ were given by Simon[13] and the general expressions were given by Shavaliev[14]. Both authors assumed the gas to be Maxwellian.

We only list the one-dimensional linear third-order terms as follows (Maxwellian gas):

$$\sigma_{11}^{(3)} = \frac{\mu^3}{p^2}\left(\frac{2}{9}RT\,u_{xxx}\right), \tag{25}$$

$$q_1^{(3)} = \frac{\mu^3}{p\rho}\left(-\frac{157}{16}RT_{xxx} - \frac{5}{8}\frac{RT}{\rho}\rho_{xxx}\right). \tag{26}$$

4. Stabilization of the Burnett Equations

For gas flows in the continuum transitional regime where Kn is the order of one, the Navier-Stokes equations become inaccurate. The second-order Burnett equations are needed as the constitutive equations to circumvent the inaccuracy of the Navier-Stokes equations. The necessity of using the Burnett equations has been demonstrated by Fiscko and Chapman[4, 5]. They found that the Burnett equations are significantly more accurate than the Navier-Stokes equations for hypersonic shock wave structure in monatomic gases.

However, the Burnett equations are known to be unstable when solved by numerical methods using fine meshes. The unstability of the equations can be shown by a linearized analysis. The analysis was reported by Bobylev[7] in 1982. In this section, we first repeat the stability analysis of Bobylev to show that the solutions of the Burnett equations are exponentially unstable to periodic perturbations when the wavelengths of the perturbations are shorter than some critical length of the order of the mean free path. Then, the same method of analysis is used to show that the Burnett equations plus some linear higher-order terms are always stable to small perturbations. These " augmented Burnett equations " are proposed in order to solve the conventional Burnett equations for practical problems numerically and to retain the accuracy of the conventional Burnett equations.

The Conventional Burnett Equations Are Unstable

We consider a simple one-dimensional problem: the response of a uniform monatomic gas to a small periodic perturbation wave. The initial gas variables are $\rho = \rho_0$, $T = T_0$, $u = u_0 = 0$. Since the perturbation is weak, the general one-dimensional governing equations (1) can be linearized to the following equations of small disturbances:

$$\rho_t + \rho\, u_x = 0 \tag{27}$$

$$u_t + \frac{RT}{\rho}\rho_x + R\,T_x + \frac{1}{\rho}\frac{\partial \sigma}{\partial x} = 0 \tag{28}$$

$$T_t + \frac{2}{3}T\,u_x + \frac{2}{3R\rho}\frac{\partial q}{\partial x} = 0 \tag{29}$$

where σ is the linearization of σ_{11} and q is the linearization of q_1 in Eq. (6).

For the Burnett equations for Maxwellian gas, the linearized terms σ and q are:

$$\sigma = -\frac{4}{3}\mu\, u_x + \frac{\mu^2}{p}\left(\alpha_7 RT_{xx} + \alpha_9\frac{RT}{\rho}\rho_{xx}\right), \tag{30}$$

$$q = -\kappa T_x + \frac{\mu^2}{\rho}\left(\gamma_3\, u_{xx}\right). \tag{31}$$

where $\alpha_7 = \frac{2}{3}$, $\alpha_9 = -\frac{4}{3}$ and $\gamma_3 = -\frac{7}{4}$ for the Maxwellian gas.

We introduce the following non-dimensional variables for the equations from Eq. (27) to (31):

$$\begin{cases} \rho' &= (\rho - \rho_0)/\rho_0 \\ T' &= (T - T_0)/T_0 \\ u' &= u/\sqrt{RT_0} \\ t' &= t/(\mu_0/p_0) \\ x' &= x/L_0 \end{cases} \tag{32}$$

where $L_0 = \mu_0/(\rho_0\sqrt{RT_0})$ is the characteristic length which is related to the hard-sphere mean free path (λ) of the gas by

$$L_0 = 0.78\,\lambda\,.$$

Substituting Eq. (32) into the equations from Eq. (27) to (31) leads the following non-dimensional perturbation equations:

$$\frac{\partial V'}{\partial t'} + \begin{bmatrix} 0 & 1 & 0 \\ 1 & 0 & 1 \\ 0 & \frac{2}{3} & 0 \end{bmatrix}\frac{\partial V'}{\partial x'} + \frac{\partial}{\partial x'}\begin{Bmatrix} 0 \\ \sigma' \\ \frac{2}{3}q' \end{Bmatrix} = 0 \tag{33}$$

where

$$V' = \left\{ \begin{array}{c} \rho' \\ u' \\ T' \end{array} \right\} \tag{34}$$

and

$$\sigma' = -\frac{4}{3}\frac{\partial u'}{\partial x'} + \left(\frac{2}{3}\frac{\partial^2 T'}{\partial x'^2} - \frac{4}{3}\frac{\partial^2 \rho'}{\partial x'^2} \right), \tag{35}$$

$$q' = -\frac{15}{4}\frac{\partial T'}{\partial x'} - \frac{7}{4}\frac{\partial^2 u'}{\partial x'^2}. \tag{36}$$

Assume the solutions of Eq. (33) with the initial perturbation $V_0' = \overline{V}\, e^{i\omega x'}$ to be:

$$V' = \overline{V}\, e^{i\omega x'} \cdot e^{\phi t'} \tag{37}$$

where the variable ω is the non-dimensional circular frequency of the periodic perturbation wave which has the following relation with wavelength L:

$$\omega = \frac{2\pi}{L/L_0} = 4.92\,\frac{\lambda}{L}. \tag{38}$$

The exponent ϕ represents the response of the governing equations to the perturbation and can be written as

$$\phi = \alpha + \beta\, i$$

where α and β are real numbers, and α represents the attenuation and β represents the dispersion. The condition for the Eq. (37) to be stable is:

$$\alpha \leq 0. \tag{39}$$

Substituting Eq. (37) into Eqs. (33), (35) and (36) leads to the following equation of characteristics for the Burnett equations:

$$\begin{aligned} p(\phi, \omega^2) = {} & 18\,\phi^3 + 69\omega^2\,\phi^2 + \\ & (30\omega^2 + 97\omega^4 - 14\omega^6)\,\phi + \\ & (45\omega^4 + 60\omega^6) \\ = {} & 0. \end{aligned} \tag{40}$$

The equation above can be solved numerically to obtain

$$\phi = f(\omega) = f(4.92\,\frac{\lambda}{L}). \tag{41}$$

From this equation, we can plot the trajectories of $\phi = \alpha + \beta\, i$ in the complex plane as L decreases from $+\infty$ to 0 (Kn increases from 0 to $+\infty$) in Figure 1, which also contains the trajectories for the Navier-Stokes equations obtained by the same method.

In Figure 1, the trajectories of the Navier-Stokes equations are always in the stable region ($\alpha \leq 0$) and move towards the negative α direction as L decreases. This means that the Navier-Stokes equations provide more attenuation as the wavelength of the perturbation decreases, which is intuitively obvious.

On the other hand, two branches of the trajectories of the Burnett equations go into the unstable region ($\alpha \geq 0$) when $L \leq L_{cr}$ ($L_{cr} = 2.04\lambda$ for Maxwellian gas), i.e., if the wavelength is smaller than L_{cr}, the Burnett equations become unstable.

A stability analysis for the two-dimensional Burnett equations also leads to the same results as those of the one-dimensional Burnett equations. The dotted lines in Figure 1 are also the characteristic trajectories of the two-dimensional Burnett equations responding to a perturbation propagating in an arbitrary direction. Therefore, the two-dimensional Burnett equations are also unstable to a disturbance of small wavelength.

The Augmented Burnett Equations Are Stable

From the preceding analysis, the Burnett equations are unstable to small-wavelength perturbations. Our goal is to stablize the Burnett equations so that the new equations meet the following requirements:

1. Be stable in the linearized stability analysis.
2. Be as accurate as the conventional second-order Burnett equations.

To satisfy the second requirement, we can only add higher order terms to stablize the conventional Burnett equations. The most natural choice would be the complete super Burnett equations. However, the super Burnett equations, like the Burnett equations, are also unstable to small perturbations when the wavelengths are smaller than some critical value. Figure 2 is the characteristic trajectories of the super Burnett equations for a Maxwellian gas. One branch of the trajectories enters the unstable region when L is small.

Therefore, we augment the Burnett equations with some terms of third-order derivatives which have the same forms as those in the super Burnett equations but have different coefficients. The Burnett equations plus the augmented terms form the new constitutive equations named "the augmented Burnett equations" as follows:

$$\left\{ \begin{array}{rcl} \sigma_{ij} & = & \sigma_{ij}^{(1)} + \sigma_{ij}^{(2)} + \sigma_{ij}^{(a)} \\ q_j & = & q_j^{(1)} + q_j^{(2)} + q_j^{(a)} \end{array} \right. \tag{42}$$

where the $\sigma_{ij}^{(1)}$, $\sigma_{ij}^{(2)}$, $q_j^{(1)}$ and $q_j^{(2)}$ are given by Section 3; $\sigma_{ij}^{(a)}$ and $q_j^{(a)}$ are the augmented terms.

One-dimensional $\sigma_{11}^{(a)}$ and $q_1^{(a)}$ are:

$$\sigma_{11}^{(a)} = \frac{\mu^3}{p^2}\left\{\omega_7 RT\, u_{xxx}\right\}, \tag{43}$$

$$q_1^{(a)} = \frac{\mu^3}{p\rho}\left\{\theta_7 R\, T_{xxx} + \theta_6 \frac{RT}{\rho}\, \rho_{xxx}\right\} \tag{44}$$

where the coefficients ω_7, θ_6 and θ_7 of the augmented terms are so selected that the new augmented Burnett equations are stable by linearized analysis. The coefficients are chosen to be those of Wang-Chang[15] for a Maxwellian gas:

$$\begin{cases} \omega_7 &= \frac{2}{9} \\ \theta_6 &= -\frac{5}{8} \\ \theta_7 &= \frac{11}{16} \end{cases} . \tag{45}$$

We obtain the characteristic equation for the one-dimensional augmented Burnett equations for Maxwellian gas as follows:

$$\begin{aligned} p(\phi,\omega^2) = \phi^3 &+ (\frac{23}{6}\omega^2 + \frac{49}{72}\omega^4)\,\phi^2 + \\ &(\frac{15}{9}\omega^2 + \frac{97}{18}\omega^4 + \frac{7}{18}\omega^6 + \frac{11}{108}\omega^8)\,\phi + \\ &(\frac{5}{2}\omega^4 + \frac{101}{24}\omega^6 + \frac{3}{9}\omega^8) \\ &= 0 . \end{aligned} \tag{46}$$

Figure 3 is the characteristic trajectories for the augmented Burnett equations. The trajectories of the new equations are always in the stable region. Therefore, the augmented Burnett equations are stable.

General $\sigma_{ij}^{(a)}$ and $q_i^{(a)}$

We have generalized the one-dimensional augmented terms in Eq. (43) and Eq. (44) to the following general expressions:

$$\sigma_{ij}^{(a)} = \frac{\mu^3}{p^2} \left\{ \frac{3}{2}\omega_7\, RT\, \overline{\frac{\partial}{\partial x_j}(\frac{\partial^2 u_i}{\partial x_k \partial x_k})} \right\} , \tag{47}$$

$$\begin{aligned} q_i^{(a)} = \frac{\mu^3}{p\rho} \Big\{ &\theta_7\, R\, \frac{\partial}{\partial x_i}(\frac{\partial^2 T}{\partial x_k \partial x_k}) + \\ &\theta_6\, \frac{RT}{\rho}\, \frac{\partial}{\partial x_i}(\frac{\partial^2 \rho}{\partial x_k \partial x_k}) \Big\} \end{aligned} \tag{48}$$

where ω_7, θ_6 and θ_7 are given by Eq. (45).

Two-dimensional $\sigma_{ij}^{(a)}$ and $q_i^{(a)}$:

From the general expressions above, we obtain the two dimensions terms as follows:

$$\begin{aligned} \sigma_{11}^{(a)} = \frac{\mu^3}{p^2} (&\omega_7\, RT\, u_{xxx} + \omega_7\, RT\, u_{xyy} \\ &- \frac{\omega_7}{2}\, RT\, v_{xxy} - \frac{\omega_7}{2}\, RT\, v_{yyy}) , \end{aligned} \tag{49}$$

$$\begin{aligned} \sigma_{12}^{(a)} &= \sigma_{21}^{(a)} \\ &= \frac{\mu^3}{p^2} (\frac{3\omega_7}{4}\, RT\, u_{xxy} + \frac{3\omega_7}{4}\, RT\, u_{yyy} \\ &\quad + \frac{3\omega_7}{4}\, RT\, v_{xyy} + \frac{3\omega_7}{4}\, RT\, v_{xxx}) , \end{aligned} \tag{50}$$

$$\begin{aligned} \sigma_{22}^{(a)} = \frac{\mu^3}{p^2} (&\omega_7\, RT\, v_{yyy} + \omega_7\, RT\, v_{xxy} \\ &- \frac{\omega_7}{2}\, RT\, u_{xyy} - \frac{\omega_7}{2}\, RT\, u_{xxx}) \end{aligned} \tag{51}$$

and

$$\begin{aligned} q_1^{(a)} = \frac{\mu^3}{p\rho} (&\theta_7\, R\, T_{xxx} + \theta_7\, R\, T_{xyy} + \\ &\theta_6\, \frac{RT}{\rho}\, \rho_{xxx} + \theta_6\, \frac{RT}{\rho}\, \rho_{xyy}) , \end{aligned} \tag{52}$$

$$\begin{aligned} q_2^{(a)} = \frac{\mu^3}{p\rho} (&\theta_7\, R\, T_{yyy} + \theta_7\, R\, T_{xxy} + \\ &\theta_6\, \frac{RT}{\rho}\, \rho_{yyy} + \theta_6\, \frac{RT}{\rho}\, \rho_{xxy}) . \end{aligned} \tag{53}$$

A stability analysis for the two-dimensional augmented Burnett equations shows that they have the same characteristic trajectories as the one-dimensional case (Figure 3), hence they are stable for all wavelengths.

The stability analysis so far has been for the simplest linear one-dimensional case only. But the nonlinear terms in the Burnett equations are important in most of the practical hypersonic applications. Therefore the linearized stability analysis provides only the necessary stability condition for the nonlinear Burnett equations. Whether the nonlinear augmented Burnett equations are stable in practical computations needs to be tested. We will test the stability properties of both the conventional Burnett equations and the augmented Burnett equations for practical numerical computations by progressly refining the computational meshes.

5. Hypersonic Shock Wave Structure

We have computed the hypersonic shock wave structure in a monatomic gas for the conventional Burnett equations and the augmented Burnett equations to test the stability of both equations and to compare their results with those by Fiscko[4].

The governing equations for this problem were given in Section 2. The computations used uniformly spaced grids. The upstream boundary conditions were specified and those in the downstream were determined by the Rankine-Hugoniot relations, hence the question of which boundary conditions are appropriate for the Burnett equations was avoided. Since the nonlinear Burnett terms became important only in the strong shock wave structure, the problem provided a good test for both the accuracy and the stability of the nonlinear Burnett equations.

For comparison purpose, the same flow conditions as Fiscko[4] were used in the computations, i.e., a monatomic gas with the molecular weight of argon was

computed for a shock wave with the following parameters:

$$\begin{cases} T_\infty &= 300\,^\circ K \\ p_\infty &= 1\,atm \\ Pr &= 2/3 \\ \gamma &= 5/3 \\ \mu &= \mu_0\,(T/T_0)^\omega \\ \mu_0 &= 0.00002272\,Ns/m^2 \\ T_0 &= 300\,^\circ K \end{cases} \tag{54}$$

where ω depends on the molecular model used in the computations. We used the same $n = 10$ exponential repulsive molecular force model as Fiscko's for gas argon; the resulting ω was as follows:

	Maxwellian	Argon	Hard-sphere
ω	1.0	0.72222	0.5

An implicit flux-splitting method[16] was used to solve the governing equations. The nonlinear terms and higher order derivative terms in the conventional Burnett equations and the augmented Burnett equations were also treated implicitly, which required solving a pentadiagonal matrix equations simultaneously for each time step. The details of the numerical formulation for the Burnett equations are not presented in this paper because of the page limitation.

Stability Test

We tested the stability of the conventional Burnett equations and the augmented Burnett equations by progressively refining the computation mesh (increasing the number of grid points within a fixed length). The computations were made for a Mach 20 shock wave in Maxwellian gas since this gas model had exhibited the most severe instabilities in Fiscko's work.

We started the computations for the shock structure from a 20-grid-point coarse mesh. The computations for both the conventional Burnett equations and the augmented Burnett equations were stable. Shock profiles were obtained for both equations. Then, we computed the same shock structure with more grid points spanning the same length. The conventional Burnett equations became unstable when the number of grid points exceeded 87 for this case. Figure 4 is the Mach number 8 temperature profile for the conventional Burnett equations in Fiscko's computations when they became unstable. The figure shows that the solutions of the conventional Burnett equations are unstable to numerical disturbances supported by the fine grid. In contrast, the computations of the augmented Burnett equations were stable for all the numbers of grid points tested (up to 6000 grid points, the largest number tested).

The maximum numbers of grid points for computational stability for the two equations are tabulated below:

Equations	max(grid points)	$\min(\frac{\Delta x}{\lambda})$
Burnett	87	0.8
A-Burnett	> 6000	< 0.01

The stability test showed that the conventional Burnett equations are unstable to short-wavelength perturbations; the augmented Burnett equations stablize the Burnett equations in the numerical computations for shock wave structures.

It is important to note that whereas the fundamental instability of the conventional Burnett equations could be circumvented by Fiscko in computations of one-dimensional shock structure at any altitude, it cannot be avoided in computations of the flow over a given body at altitudes above a certain height. Shock computations are made with an essentially constant $\Delta x/\lambda_\infty$ somewhat greater than the minimum critical value for stability. Both the shock thickness and the mean-free-path λ_∞, increase proportionally with increasing altitude, so that such computations apply to any altitude no matter how high. For a body of fixed dimensions, however, the grid spacing Δx for a required resolution does not increase with altitude, but stays fixed; hence $\Delta x/\lambda_\infty$ decreases steadily with increasing altitude, eventually becomes less than the minimum critical value for stability at altitudes above a certain value. The inherent instability of the conventional Burnett equations must be overcome if practical computations are to be made at high altitudes. Therefore the augmented Burnett equations are needed to overcome this difficulty.

Shock Thickness Comparison

We next computed the argon shock wave structure for Mach numbers ranging from 1.59 to 50.0. The shock inverse density thickness of the augmented Burnett equations were compared with Fiscko's results of the conventional Burnett equations and the DSMC.

Figure 5 shows the inverse density thickness of shock waves at Mach numbers ranging from 1.59 to 50.0 for argon gas. The inverse density thickness of the augmented Burnett equations agrees well with Fiscko's Burnett results. As pointed out by Fiscko, the results of the Burnett equations are always closer to DSMC than the Navier-Stokes equations. The results show that the augmented Burnett equations maintain the second order accuracy of the conventional Burnett equations for computing shock wave structure.

6. Flows Past Two-Dimensional Cylinders

We have extended the computations for the one-dimensional shock wave structure to plane-two-dimensional flows. The first problem was supersonic and hypersonic flows past cylindrical leading edges. We computed and compared the Navier-Stokes flow field with the Burnett flow field using the same set of surface boundary conditions. At the same time, we tested

the computational stability of both the conventional and augmented Burnett equations by computing them with progressively refined meshes.

The Two-Dimensional Governing Equations

The conservation equations for two-dimensional compressible flows with the rotational energy mode being in equilibrium with the translational mode and the other internal modes being frozen are:

$$\frac{\partial U}{\partial t} + \frac{\partial F}{\partial x} + \frac{\partial G}{\partial y} = 0 \tag{55}$$

where

$$U = \left\{ \begin{array}{c} \rho \\ \rho u \\ \rho v \\ e \end{array} \right\},$$

$$F = \left\{ \begin{array}{c} \rho u \\ \rho u^2 + p + \sigma_{11} \\ \rho uv + \sigma_{12} \\ (e + p + \sigma_{11})\, u + \sigma_{12} v + q_1 \end{array} \right\},$$

$$G = \left\{ \begin{array}{c} \rho v \\ \rho uv + \sigma_{21} \\ \rho v^2 + p + \sigma_{22} \\ (e + p + \sigma_{22})\, v + \sigma_{21} u + q_2 \end{array} \right\}.$$

For air, $\gamma = 1.4$, $Pr = 0.72$ and the viscosity coefficient μ was computed by the Sutherland relation.

For simplicity, thermal reactions and vibrational energy relaxation are not considered in this investigation, since the Burnett terms affect only the contribution of the translational molecular energy to the nonlinear stress-strain tensor and heat-flux vector; and it is these terms which primarily determine the stability or instability of the whole equation set.

The Navier-Stokes equations, the conventional Burnett equations and the augmented Burnett equations were computed for each case in order to compare one with the other. The three equations are different only in their constitutive equations. The constitutive equations of the Navier-Stokes equations are given by Eq. (6) with $n = 1$; The constitutive equations of the conventional Burnett equations are also given by Eq. (6) with $n = 2$; and those of the augmented Burnett equations are given by Eq. (42).

The Numerical Method

Figure 6 shows a typical body-fitted computational mesh for the flows. The finite volume method was used in all the computations. In the figure, (ξ, η) are the curvilinear computational coordinates, where the coordinates of the grid lines are $\xi = 1, \cdots, IL$ and $\eta = 1, \cdots, JL$.

In the computations, the governing equations and constitutive equations in Cartesian coordinate (x, y, t) were transformed into the curvilinear computational coordinates (ξ, η, τ). The details of the transformation are not presented in this paper, except the transformation equations for the first, second and third derivatives appearing in the constitutive equations, which are given in the appendix.

The implicit line Gauss-Seidel iteration method proposed by MacCormack for the Navier-Stokes equations[17] was used to solve the Burnett equations as well as the Navier-Stokes equations. The inviscid terms were computed by the flux-splitting method and all the viscous terms were computed by central differencing approximations. At each time step, the flow variables along η-grid lines were solved implicitly, which required the solution of a pentadiagonal matrix equation simultaneously; while the ξ-direction terms were computed by the line Gauss-Seidel iteration with alternating sweeps in the backward and forward ξ-directions.

The Boundary Conditions

Free stream conditions were specified along the top boundary ($\eta = JL$). Symmetry conditions were used along the stagnation streamline ($\xi = 1$). First-order extrapolation of the interior data was used to determined the flow variables along the exit boundary ($\xi = IL$)

For the boundary mesh points along the body surface ($\eta = 1$), the flows variables on the surface were computed by the first-order Maxwell/Smoluchowski[18, 19] slip boundary conditions (Cartesian coordinates):

$$u_s = \frac{2 - \overline{\sigma}}{\overline{\sigma}} \bar{l} \left(\frac{\partial u}{\partial y}\right)_s + \frac{3}{4} \frac{\mu}{\rho T} \left(\frac{\partial T}{\partial x}\right)_s \tag{56}$$

and

$$T_s = T_w + \frac{2 - \overline{\alpha}}{\overline{\alpha}} \frac{2\gamma}{\gamma + 1} \frac{\bar{l}}{Pr} \left(\frac{\partial T}{\partial y}\right)_s, \tag{57}$$

where

$$\bar{l} = \frac{2\mu}{\rho} \sqrt{\frac{\pi}{8RT}}.$$

The subscript s represents the flow variables on the surface and T_w is the temperature of the surface body. $\overline{\sigma}$ is the reflection coefficient and $\overline{\alpha}$ is the accommodation coefficient. For this study, complete accommodation was assumed, i.e. , $\overline{\sigma} = 1$ and $\overline{\alpha} = 1$.

In the case of the Burnett equations, evaluations of the second and third order derivatives were needed on the body surface. We used one-sided difference to evaluate these higher order derivatives on the surfaces.

At the present stage of this research, the same slip boundary conditions were used for both the Navier-Stokes equations and the Burnett equations. The question of which particular set of surface boundary conditions is the best, or the most appropriate, for the

Burnett equations is an important one, but is outside the scope of the present paper.

It was noted that Tannehill and Eisler[20] solved the two-dimensional Burnett equations in 1976 for a hypersonic flow over a flat plate with sharp leading edge, which was the first two-dimensional attempt with these equations. Their computations were necessarily restricted to a coarse mesh because of computer limitations at that time. The evenly spaced mesh sizes in their computations corresponded to $\Delta x/\lambda_\infty = 4.8$ and $\Delta y/\lambda_\infty = 1.9$, which are larger than the minimum value $\Delta x/\lambda_1 = 0.8$ for shock computation stability. Therefore, their computations may not have run into an instability problem because of the relatively coarse mesh used. It is also noted that they used different surface boundary conditions for Burnett (Schamberg[21]) than for Navier-Stokes (Maxwell/Smoluchowski [19]), and obtained results for Burnett that appeared worse than for Navier-Stokes. In contrast, one-dimensional hypersonic shock structure tests, which involve no uncertainty about boundary conditions, have shown the Burnett results to be much better than the Navier-Stokes. The reason for this apparent difference is not understood at present. It may or may not be associated with boundary conditions.

Case I. (Low Altitude, $M_\infty = 4.0$)

The flow conditions of the first case were the same as those of the experimental test by Kim[22], [23] for supersonic air flow past a cylinder:

$$\begin{cases} M_\infty &= 4.0 \\ Re_\infty &= 9.1 \times 10^4 \\ Kn_\infty &= 0.67 \times 10^{-4} \end{cases}$$

where

$$Kn_\infty = \frac{\lambda_\infty}{r},$$

$$Re_\infty = \frac{\rho_\infty u_\infty r}{\mu_\infty}$$

and r is the radius of the test cylinder.

Since $Kn_\infty \ll 1.0$, the flow belonged to the continuum regime and therefore could be accurately described by the Navier-Stokes equations (except in the negligibly thin region within the bow shock wave). The Burnett equations were expected to yield the same results as the Navier-Stokes equations. This case was also a test case for our newly written two-dimensional implicit computer code for the Navier-Stokes, the original Burnett equations and the augmented Burnett equations.

The computational mesh for this case is shown in Figure 6. The mesh lines are aligned with the boundary surfaces and the predicted shock shape.

Figure 7 shows the results for the shape of the bow shock wave. The experimental bow shock shape agrees well with the shape from the Navier-Stokes equations and from the Burnett equations.

Figures 8 and 9 are the density and pressure distributions along the stagnation streamline. The results of the Navier-Stokes equations are compared with those from the Burnett equations with the same surface boundary conditions. The results of the two equations are essentially the same except for slight differences in the small region within the bow shock. This is because the strong compression across the shock increases the local Knudson number within the shock wave, hence the magnitudes of the Burnett terms in the shock region increase.

Figures 10, 11,12 and 13 show the density and pressure contours for the Navier-Stokes equations and the Burnett equations. The corresponding contours of the two sets of equations agree well with each other.

From these results, we see that the Burnett equations give essentially the same results as the Navier-Stokes equations at low altitudes ($Kn_\infty \ll 1$).

We next computed the air flows of $M_\infty = 10.0$ past a cylinder of radius $r = 0.02\,m$. The computed cases covered the whole continuum transitional regime from low altitudes to high altitudes as follows: $0\ km$ (sea level), $65\ km$, $75\ km$, $80\ km$, $90\ km$ and $95 km$. The corresponding free-stream Knudsen numbers were from 3.3×10^{-6} to 2.3. In this paper, we present the two typical cases: the flows at the altitudes of $75\ km$ and $90\ km$.

Case II. (Attitude = $75\,km$, $M_\infty = 10.0$)

The flow parameters for this case were

$$\begin{cases} \text{Altitude} &= 75\ km \\ M_\infty &= 10.0 \\ Kn_\infty &= 0.102 \\ Re_\infty &= 167.9 \\ r &= 0.02\ m \\ T_w &= 1000.0\ ^\circ K \end{cases}$$

The Kundsen number increased from 0.67×10^{-4} of Case I to $Kn = 0.102$ for this case, in which the flow begins to depart from the continuum regime and enters the transitional regime. The Navier-Stokes equations become inaccurate and the Burnett solutions become different from the Navier-Stokes solutions.

Figure 14 is the computational mesh of 40×62 grid points for this case. Because the shock wave thickness was a sizable part of the shock detachment distance, the grid was evenly spaced along the stagnation streamline and the solid surface.

Stability of the Burnett equations: The computations for the conventional Burnett equations and the augmented Burnett equations were stable for this case with the 40×62 grid points mesh. The free-stream Kundsen number based on the minimum grid size was $Kn_{\Delta x\infty} = 8.1$. When we refined the mesh by increasing the number of grid points to 78×122 within

the same computational domain, the computations for the conventional Burnett equations became unstable, while the computations for the augmented Burnett equations remained stable. Therefore the approximate maximum $Kn_{\Delta x\infty}$ for two-dimensional conventional Burnett equations computations to be stable is near $Kn_{\Delta x\infty} = 8.1$. The computations in this case as well as those in the following cases showed that the augmented Burnett equations stablize the conventional Burnett equations in two dimensions.

The Burnett Flow Field Compared with the Navier-Stokes Flow Field: Figures 15, 16 and 17 are density, velocity and temperature distributions along the stagnation streamline. In both figures, the results of the Navier-Stokes equations, the conventional Burnett equations and the augmented Burnett equations are plotted on the same figures. The difference between the Burnett equations and Navier-Stokes equations are evident, especially for the temperature distribution across the shock. Meanwhile, the results of the augmented Burnett equations agree well with the conventional Burnett equations. Hence, the augmented Burnett equations do maintain the accuracy of the conventional Burnett equations when the solutions of the later equations are possible.

Figures 18, 19, 20 and 21 show the density and temperature contours for the Navier-Stokes equations and the Augmented Burnett equations. The two-dimensional augmented Burnett equations result in a thicker bow shock wave.

Case III. (Attitude = 90 km , $M_\infty = 10.0$)

The flow parameters for this case were:

$$\begin{cases} \text{Altitude} &= 90\ km \\ M_\infty &= 10.0 \\ Kn_\infty &= 1.185 \\ Re_\infty &= 14.9 \\ r &= 0.02\ m \\ T_w &= 1000.0\,^\circ K \end{cases}$$

The Kundsen number was 1.185 and the flow was well into the continuum transitional regime in this case. The Navier-Stokes equations are inaccurate and the Burnett solutions become significantly different from the Navier-Stokes solutions.

A computational mesh for this case was similar to Figure 14 with 40 × 142 grid points. The minimum mesh size was the same as that of Figure 14. A larger computational domain was used because the bow shock wave stretched farther upstream for the large Kundsen number flow.

Stability of the Burnett equations: The computations for the Navier-Stokes and the augmented Burnett equations were stable, whereas the computations for conventional Burnett equations were unstable. The free-stream Kundsen number based on the minimum grid size was $Kn_{\infty\Delta x} = 94.8$. These results showed the augmented Burnett equations stablize the conventional Burnett equations in two dimensions, up to very high altitudes.

The Burnett Flow Field Compared with the Navier-Stokes Flow Field: Figures 22, 23 and 24 are density , velocity and temperature distributions along the stagnation streamline. The difference between the augmented Burnett equations and Navier-Stokes equations become significant in this case, especially for the temperature distribution across the shock. This may have a significant effect on properties sensitive to flow field details, such as radiation heating.

Figures 25, 26, 27 and 28 show the density and temperature contours for the Navier-Stokes equations and the Augmented Burnett equations. The two-dimensional augmented Burnett equations result in much thicker bow shock wave.

7. 2D Hypersonic Flow Past a Double Ellipse

In this section, we computed hypersonic $M_\infty = 25$ air flows past a double ellipse geometry in the transitional regime. The same problem was computed by Feiereisen[24] using the particle simulation method of Baganoff. In Feiereisen's computations, hard-sphere model and a rotational nonequilibrium model of collision number 2 were used. We used the same models to compute the flow and compared the results of the Navier-Stokes equations and the Burnett equations with Feiereisen's.

The case had very low T_∞ and a cold wall, therefore the vibrational mode of the air flow was assumed to be frozen and only translational and rotational nonequilibrium needed to be considered for this case.

Though the Burnett equations were derived for the monatomic gas only, Lumpkin[10] demonstrated that the Burnett equations plus rotational nonequilibrium model provide satisfactory shock wave structure for a diatomic gas such as nitrogen. Therefore, we used the Burnett equations for both the viscous stress and translational heat transfer and used first order equations for the rotational heat transfer.

The Governing Equations

The conservation equations for the two-dimensional flows with rotational nonequilibrium are:

$$\frac{\partial U}{\partial t} + \frac{\partial F}{\partial x} + \frac{\partial G}{\partial y} = W \tag{58}$$

where

$$U = \begin{Bmatrix} \rho \\ \rho u \\ \rho v \\ e_r \\ e \end{Bmatrix},$$

$$F = \left\{ \begin{array}{c} \rho u \\ \rho u^2 + p + \sigma_{11} \\ \rho uv + \sigma_{12} \\ e_r\, u + q_{r1} \\ (e + p + \sigma_{11})\, u + \sigma_{12} v + q_1 + q_{r1} \end{array} \right\} ,$$

$$G = \left\{ \begin{array}{c} \rho v \\ \rho uv + \sigma_{21} \\ \rho v^2 + p + \sigma_{22} \\ e_r\, v + q_{r2} \\ (e + p + \sigma_{22})\, v + \sigma_{21} u + q_2 + q_{r2} \end{array} \right\} ,$$

$$W = \left\{ \begin{array}{c} 0 \\ 0 \\ 0 \\ \omega_r \\ 0 \end{array} \right\} ,$$

$$e_r = \rho c_{vr} T_r ,$$

$$c_{vr} = R ,$$

$$e = e_r + \rho \left(c_{vt} T + \frac{u^2 + v^2}{2} \right) ,$$

$$c_{vt} = \frac{3R}{2}$$

and T is the translational temperature; T_r is the rotational temperature. The stress σ_{ij} and translational heat transfer q_i are given in the preceding sections.

The rotational heat flux terms q_{ri} are as follows:

$$q_{ri} = -\kappa_r \frac{\partial T_r}{\partial x_i} . \tag{59}$$

where the rotational heat conductivity κ_r and translational heat conductivity κ for diatomic gases are approximated by the Eucken's relation[25]:

$$\left\{ \begin{array}{rcl} \kappa & = & 5 \mu c_{vt} / 2 \\ \kappa_r & = & \mu c_{vr} \end{array} \right. . \tag{60}$$

Like the particle simulation by Feiereisen, we used hard-sphere gas model in the computations. The viscosity for hard-sphere gas is:

$$\mu = \mu_0 \left(\frac{T}{T_0} \right)^{0.5} . \tag{61}$$

The following rotational relaxation model was used in the computations:

$$\omega_r = \rho \frac{c_{vr} (T - T_r)}{Z_R \tau_c} \tag{62}$$

with

$$\tau_c = \frac{\pi \mu}{4p}$$

and

$$Z_R = 2$$

where the rotation collision number Z_R was the same as in the particle simulation.

The Numerical Method and Boundary Conditions

The same numerical method and boundary conditions as in Section 6 were used in the computations, with slightly different surface-slip boundary conditions because of the rotational nonequilibrium. The first-order Maxwell/Smoluchowski slip boundary conditions were extended to rotational nonequilibrium[18] as follows (Cartesian coordinates):

$$u_s = \frac{2 - \overline{\sigma}}{\overline{\sigma}} \overline{l} \left(\frac{\partial u}{\partial y} \right) + \frac{3}{4} \frac{\mu}{\rho T} \left(\frac{\partial T}{\partial x} \right) \tag{63}$$

$$T_s = T_w + \frac{2 - \overline{\alpha}}{\overline{\alpha}} \frac{3 \kappa_t}{2 \rho \overline{c}\, c_{vt}} \left(\frac{\partial T}{\partial y} \right) \tag{64}$$

$$T_{rs} = T_w + \frac{2 - \overline{\alpha}}{\overline{\alpha}} \frac{2 \kappa_r}{\rho \overline{c}\, c_{vr}} \left(\frac{\partial T_r}{\partial y} \right) \tag{65}$$

where

$$\overline{c} = \sqrt{\frac{8RT}{\pi}} .$$

In the computations, complete accommodation surface was assumed, i.e., $\overline{\sigma} = 1$ and $\overline{\alpha} = 1$, which were the same as in the particle simulation.

Case IV. : Double Ellipse Flow ($M_\infty = 25.0$, Angle of Attack = 30 °)

The flow conditions of the case were:

$$\left\{ \begin{array}{rcl} M_\infty & = & 25.0 \\ Kn_\infty & = & 0.28 \\ \text{Angle of Attack} & = & 30\,^\circ \\ \lambda_\infty & = & 1.05 \times 10^{-3}\, m \\ T_\infty & = & 13.5\,^\circ K \\ T_w & = & 620.0\,^\circ K \\ \text{Nose Radius} & = & 0.00375\, m \end{array} \right. .$$

Figure 29 shows the body-fitted computational grid of 68 x 62 grid points for the double ellipse geometry.

Stability of the Burnett equations: The computations for the Navier-Stokes and the augmented Burnett equations were stable, while the computations for conventional Burnett equations were unstable. These results again showed that the augmented Burnett equations stablize the conventional Burnett equations in two dimensions.

The Burnett Flow Field and the Navier-Stokes Flow Field Compared with the Particle Simulation: Figures 30, 31 and 32 are density, velocity and translational temperature distributions along the stagnation line. The results are compared with the particle simulation

results. In both figures, the results of the augmented Burnett equations agree better with those of the particle simulation than those of the Navier-Stokes equations. The results indicate the Burnett equations to be more accurate than the Navier-Stokes equations. It should be pointed out that the difference between the Navier Stokes flow field and the Burnett flow field is not large because the Kundsen number of the flow was about 0.28 and the artificial hard-sphere model was used in the computations. Still the two-dimensional augmented Burnett equations result in a thicker bow shock wave and agree very well with the particle simulation results.

Figures 33 shows the rotational and translational temperature along the stagnation line. The rotational temperature lags behind the translational temperature across the shock wave.

Figures 34, 35, 36 and 37 are the density and translational temperature contours for the case. The density contours of the augmented Burnett equations and the Feiereisen's results are plotted together for comparison. The figures show the density and temperature contours for the Augmented Burnett equations agree well with the particle simulation results.

8. Conclusions

A new set of equations termed the "augmented Burnett equations" has been developed which overcome the instability of the conventional Burnett equations to small wavelength perturbations. We have computed both 1D shock wave structures and 2D flows past blunt leading edges using the new equations. The analytical analysis and numerical test cases have demonstrated the following properties of the new equations:

1. The augmented Burnett equations are always stable in the theoretical analysis as well as in both the 1D and 2D numerical computation tests produced to date.

2. The new equations maintain the same accuracy as the conventional Burnett equations.

3. At low altitudes ($Kn \leq 0.1$), the difference between the 2D computational results of the Burnett equations and those of the Navier-Stokes equations is small.

4. At high altitudes ($Kn \approx O(1)$), the difference between the 2D computational results (especially T) of the Burnett equations and those of the Navier-Stokes equations is significant, which makes it preferable to use the Burnett equations instead of the Navier-Stokes equations in this regime. Burnett CFD appears to be especially important for predicting aerodynamic parameters sensitive to flow-field details, such as radiation.

5. Computation times with the Burnett equations are only modestly greater than Navier-Stokes with the same grid system; The Burnett solutions required about 40-percent more CPU time than Navier-Stokes for both the 1D and 2D flows investigated.

9. Acknowledgements

This research was supported by SDIO/IST managed by the Army Research Office under contracts DAAL03-86K-0139 and DAAL03-90-G-0031-P00002. We would also like to acknowledge the Aerothermodynamics Branch of NASA Ames Research Center for providing computer time on the Cray-YMP computer.

10. Appendix

The Derivative Transformation Equations

The equations of the grid transformation are:

$$\begin{cases} x &= x(\xi, \eta, \tau) \\ y &= y(\xi, \eta, \tau) \\ t &= \tau \end{cases} \tag{66}$$

The transformation equations for the derivatives from curvilinear coordinates (ξ, η, τ) to Cartesian coordinates (x, y, t) can be derived by the chain rules.

The first-order derivative transformation equations are:

$$\frac{\partial}{\partial x} = a \frac{\partial}{\partial \xi} + b \frac{\partial}{\partial \eta} \tag{67}$$

$$\frac{\partial}{\partial y} = c \frac{\partial}{\partial \xi} + d \frac{\partial}{\partial \eta} \tag{68}$$

where

$$\begin{cases} a &= y_\eta / J \\ b &= -y_\xi / J \\ c &= -x_\eta / J \\ d &= x_\xi / J \\ J &= x_\xi y_\eta - x_\eta y_\xi \end{cases}$$

The second-order derivative transformation equations are:

$$\frac{\partial^2}{\partial x^2} = a^2 \frac{\partial^2}{\partial \xi^2} + 2ab \frac{\partial^2}{\partial \xi \partial \eta} + b^2 \frac{\partial^2}{\partial \eta^2} + a_x \frac{\partial}{\partial \xi} + b_x \frac{\partial}{\partial \eta} \tag{69}$$

$$\frac{\partial^2}{\partial x \partial y} = ac \frac{\partial^2}{\partial \xi^2} + (ad + bc) \frac{\partial^2}{\partial \xi \partial \eta} + bd \frac{\partial^2}{\partial \eta^2} + c_x \frac{\partial}{\partial \xi} + d_x \frac{\partial}{\partial \eta} \tag{70}$$

$$\frac{\partial^2}{\partial y^2} = c^2 \frac{\partial^2}{\partial \xi^2} + 2cd \frac{\partial^2}{\partial \xi \partial \eta} + d^2 \frac{\partial^2}{\partial \eta^2} + c_y \frac{\partial}{\partial \xi} + d_y \frac{\partial}{\partial \eta} \tag{71}$$

where the coefficients such as a_x and d_y can be computed by Eq. (67) and (68).

The third-order derivative transformation equations are

$$\frac{\partial^3}{\partial x^3} = a^3 \frac{\partial^3}{\partial \xi^3} + 3a^2 b \frac{\partial^3}{\partial \xi^2 \partial \eta} + b^3 \frac{\partial^3}{\partial \eta^3} + 3ab^2 \frac{\partial^3}{\partial \xi \partial \eta^2} + 3a\, a_x \frac{\partial^2}{\partial \xi^2} + 3b\, b_x \frac{\partial^2}{\partial \eta^2} + 3(a\, b_x + b\, a_x) \frac{\partial^2}{\partial \xi \partial \eta} + a_{xx} \frac{\partial}{\partial \xi} + b_{xx} \frac{\partial}{\partial \eta} \tag{72}$$

$$\frac{\partial^3}{\partial x^2 \partial y} = a^2 c \frac{\partial^3}{\partial \xi^3} + (2abc + a^2 d) \frac{\partial^3}{\partial \xi^2 \partial \eta} + b^2 d \frac{\partial^3}{\partial \eta^3} + (b^2 c + 2abd) \frac{\partial^3}{\partial \xi \partial \eta^2} + (ca_x + 2aa_y) \frac{\partial^2}{\partial \xi^2} + (db_x + 2bb_y) \frac{\partial^2}{\partial \eta^2} + (c\, b_x + d\, a_x + 2a_y\, b + 2a\, b_y) \frac{\partial^2}{\partial \xi \partial \eta} + a_{xy} \frac{\partial}{\partial \xi} + b_{xy} \frac{\partial}{\partial \eta} \tag{73}$$

$$\frac{\partial^3}{\partial x \partial y^2} = c^2 a \frac{\partial^3}{\partial \xi^3} + (2acd + bc^2) \frac{\partial^3}{\partial \xi^2 \partial \eta} + bd^2 \frac{\partial^3}{\partial \eta^3} + (ad^2 + 2cdb) \frac{\partial^3}{\partial \xi \partial \eta^2} + (ac_y + 2cc_x) \frac{\partial^2}{\partial \xi^2} + (bd_y + 2dd_x) \frac{\partial^2}{\partial \eta^2} + (a\, d_y + b\, c_y + 2c_x\, d + 2c\, d_x) \frac{\partial^2}{\partial \xi \partial \eta} + c_{xy} \frac{\partial}{\partial \xi} + d_{xy} \frac{\partial}{\partial \eta} \tag{74}$$

$$\frac{\partial^3}{\partial y^3} = c^3 \frac{\partial^3}{\partial \xi^3} + 3c^2 d \frac{\partial^3}{\partial \xi^2 \partial \eta} + d^3 \frac{\partial^3}{\partial \eta^3} + 3cd^2 \frac{\partial^3}{\partial \xi \partial \eta^2} + 3c\, c_y \frac{\partial^2}{\partial \xi^2} + 3d\, d_y \frac{\partial^2}{\partial \eta^2} + 3(c\, d_y + d\, c_y) \frac{\partial^2}{\partial \xi \partial \eta} + c_{yy} \frac{\partial}{\partial \xi} + d_{yy} \frac{\partial}{\partial \eta} \tag{75}$$

where the coefficients such as a_{xx}, c_{xy} and d_{yy} can be computed by Eq. (69), (70) and (71).

References

[1] G. A. Bird. Monte Carlo simulation of gas flows. *Ann. Rev. Fluid Mech.*, 10:11–13, 1978.

[2] D. Baganoff. Vectorization of a particle code used in the simulation of rarefied hypersonic flow. *Symposium on Computational Technology for Flight Vehicles, Washington, D. C.*, November 1990.

[3] D. Baganoff and J. D. McDonald. A collision-selection rule for a particle simulation method suited to vector computers. *Physics of Fluids A*, July 1990.

[4] Kurt A. Fiscko. *Study of Continuum Higher Closure Models Evaluated by a Statistical Theory of Shock Structure.* PhD thesis, Stanford University, 1988.

[5] Kurt A. Fiscko and Dean R. Chapman. Comparison of Burnett, Super-Burnett, and Monte Carlo solutions for hypersonic shock structure. In *16th International Symposium of Rarefied Gas Dynamics*, 1988.

[6] S. Chapman and T. G. Cowling. *The Mathematics Theory of Non-Uniform Gases.* Cambridge University Press, 1960.

[7] A. V. Bobylev. The Chapman-Enskog and Grad methods for solving the Boltzmann equation. *Sov. Phys. Dokl.*, 27(1), January 1982.

[8] J. D. Foch. On higher order hydrodynamic theories of shock structure. *Acta physical Austriaca, suppl. X.*, 123–140, 1973.

[9] C. S. Wang Chang and G. E. Uhlenbeck. On the transport phenomena in rarefied gases. *Studies in Statistical Machanics*, V:1–17, 1948.

[10] F. E. Lumpkin III. *Development and Evaluation of Continuum Models for Translational-Rotational Nonequilibrium.* PhD thesis, Stanford University, March 1990.

[11] L. C. Woods. Transport processes in dilut gases over the whole range of Knudsen number. part 1. general theory. *J. of Fluid Mechanics*, 93(3):585–607, 1979.

[12] L. C. Woods. On the thermodynamics of nonlinear constitutive relations in gasdynamics. *J. of Fluid Mechanics*, 101(2):225–242, 1980.

[13] C. E. Simon. *Theory of Shock Structure in a Maxwell Gas Based on the Chapman-Enskog Development Through Super-Burnett Order.* PhD thesis, University of Colorado, 1976.

[14] M. Sh. Shavaliev. The Burnett approximation of the distribution function and the supper-Burnett contributions to the stress tensor and the heat flux. *Journal of Applied Mathematics and Mechanics*, 42(4):656–702, 1978.

[15] C. S. Wang Chang. On the theory of the thickness of weak shock waves. *Studies in Statistical Machanics*, V:27–42, 1948.

[16] J. Stager and R. F. Warming. *Flux Vector Splitting of the Inviscid Gasdynamics Equations with Application to Finite Difference Methods.* TM 78650, NASA, 1979.

[17] R. W. MacCormack. *Current Status of Numerical Solution of the Navier-Stokes Equations.* AIAA Paper 85-0032, AIAA, January 1985.

[18] E. H. Kennard. *Kinetic Theory of Gases.* McGraw-Hill Book Co., Inc., New York, 1938.

[19] Samuel A. Schaaf and P. L. Chambre. Flow of rarefied gases. *Princeton Aeronautical Paperbacks*, 8, 1961.

[20] J. C. Tannehill and R. G. Eisler. Numerical computation of the hypersonic leading edge problem using the Burnett equations. *The Physics of Fluids*, 19(1):9–15, 1976.

[21] R. Schamberg. *The Fundamental Differential Equations and the Boundary Conditions for High Speed Slip Flow.* PhD thesis, California Institute of Technology, Pasadena, California, 1947.

[22] Chul-Soo Kim. Experimental studies of supersonic flow past a circular cylinder. *J. of Physical Society of Japan*, 11(4):439–445, April 1956.

[23] W. D. Hayes and R. F. Probstein. *Hypersonic Flow Theory.* Volume I, Academic Press, New York and London, second edition, 1966.

[24] W. J. Feiereisen. The hypersonic double ellipse in rarefied flow (problem 6.4). *INRIA Workshop on Hypersonic Flows for Reentry Problems, Antibes, France 22-26, January*, 1990.

[25] W. G. Vincenti and W. G. Kruger Jr. *Introduction to Physical Gas Dynamics.* Krieg, 1965.

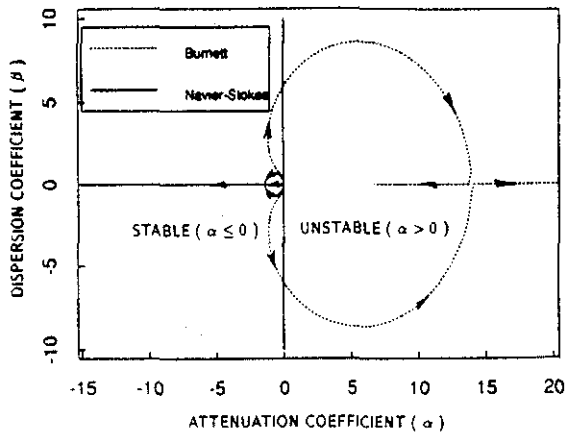

Figure 1: Maxwellian gas characteristic trajectories for flows in both one and two dimensions. The arrows show the direction in decreasing wavelength.

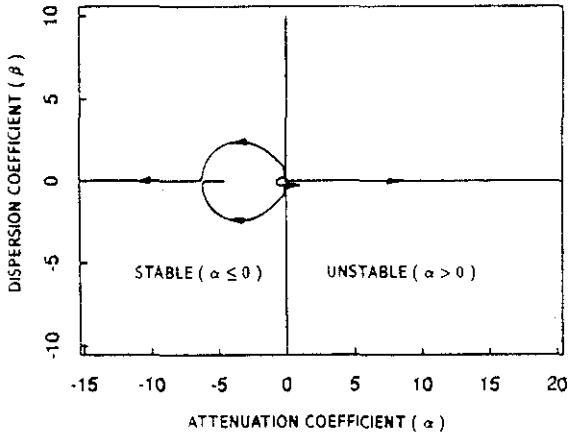

Figure 2: Maxwellian gas characteristic trajectories for the super Burnett equations. The arrows show the direction in decreasing wavelength.

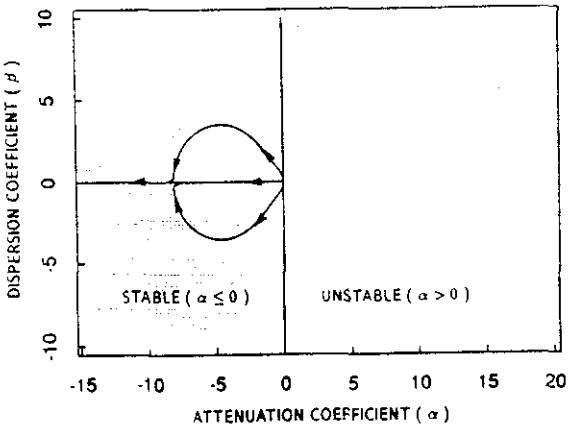

Figure 3: Maxwellian gas characteristic trajectories for the augmented Burnett equations in both one and two dimensions. The arrows show the direction in decreasing wavelength.

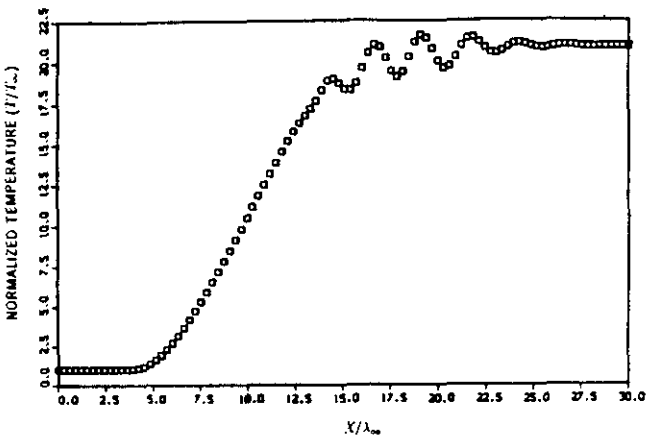

Figure 4: Shock temperature profile in Fiscko's computations of the Burnett equations when the instability started. (Maxwellian gas $M = 8$)

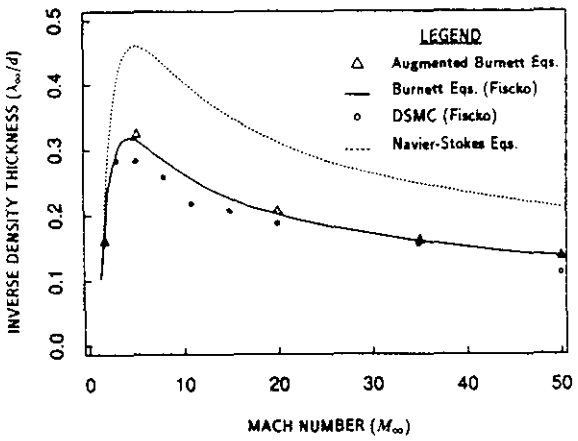

Figure 5: Argon shock wave inverse density thickness.

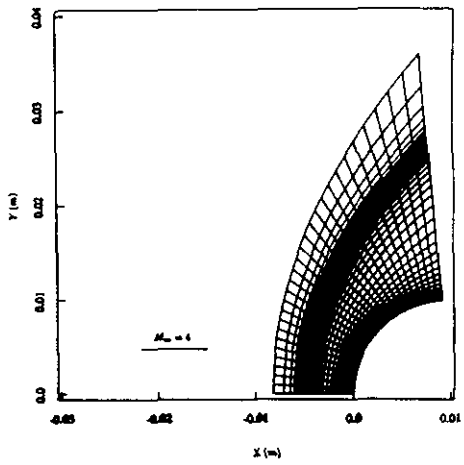

Figure 6: Computational mesh for Case I: $M_\infty = 4.0$, $Kn_\infty = 0.67 \times 10^{-4}$.

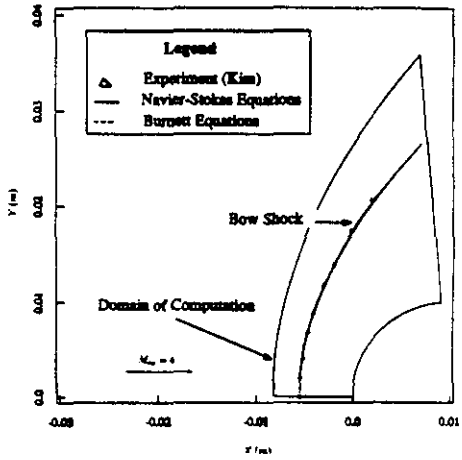

Figure 7: The bow shock shape for Case I: $M_\infty = 4.0$, $Kn_\infty = 0.67 \times 10^{-4}$.

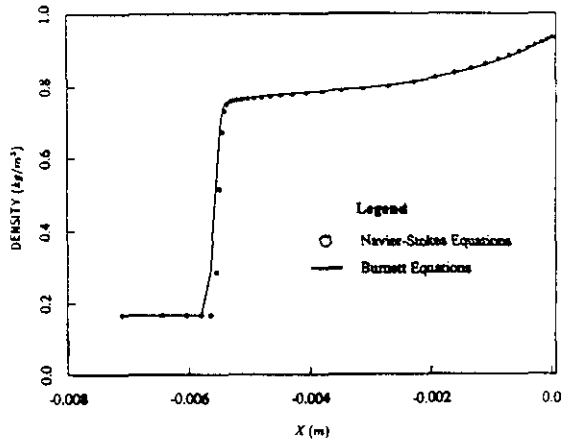

Figure 8: Density along stagnation streamline for Case I: $M_\infty = 4.0$, $Kn_\infty = 0.67 \times 10^{-4}$.

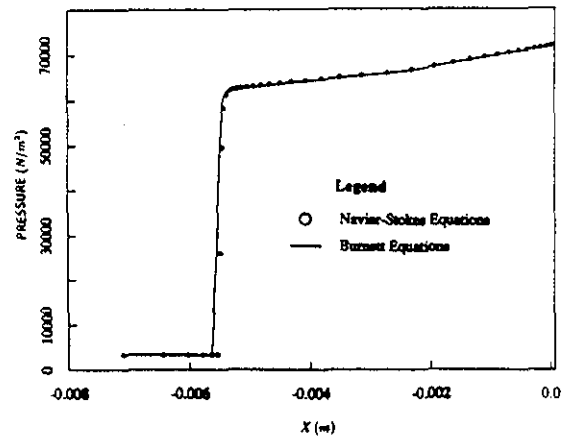

Figure 9: Pressure along stagnation streamline for Case I: $M_\infty = 4.0$, $Kn_\infty = 0.67 \times 10^{-4}$.

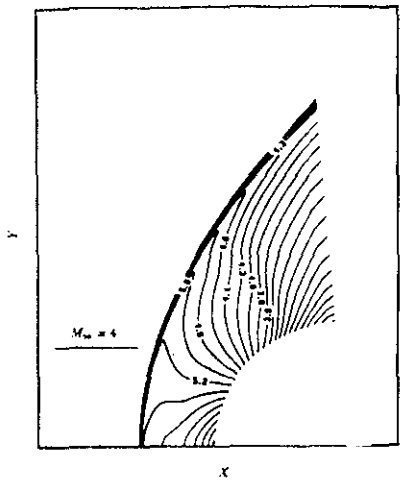

Figure 10: Navier-Stokes normalized density contours for Case I: $M_\infty = 4.0$, $Kn_\infty = 0.67 \times 10^{-4}$.

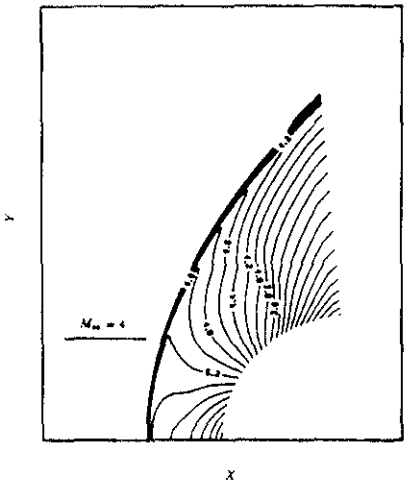

Figure 11: Burnett normalized density contours for Case I: $M_\infty = 4.0$, $Kn_\infty = 0.67 \times 10^{-4}$.

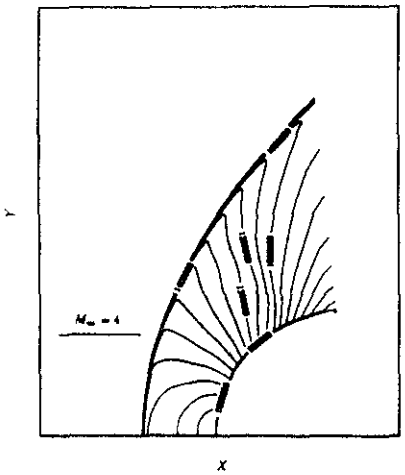

Figure 12: Navier-Stokes pressure contours for Case I: $M_\infty = 4.0$, $Kn_\infty = 0.67 \times 10^{-4}$.

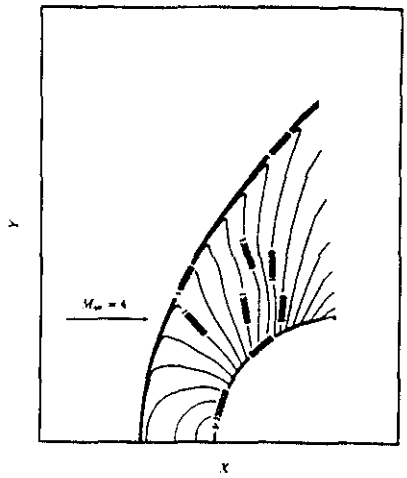

Figure 13: Burnett pressure contours for Case I: $M_\infty = 4.0$, $Kn_\infty = 0.67 \times 10^{-4}$.

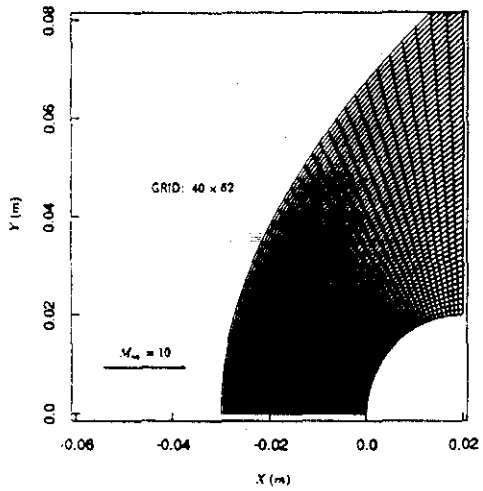

Figure 14: Computational mesh for Case II: $M_\infty = 10$, $Kn_\infty = 0.1$ and Altitude $= 75\,km$.

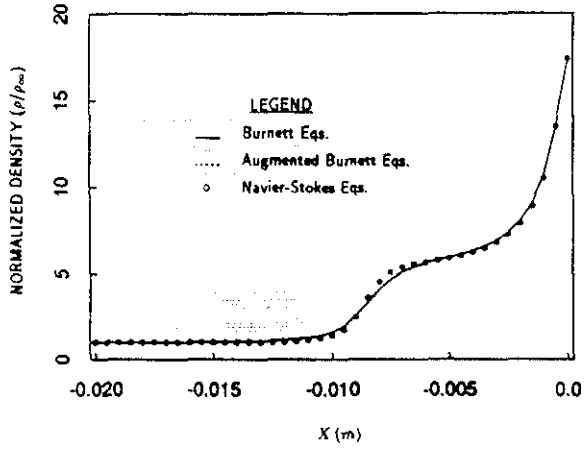

Figure 15: Density along stagnation streamline for Case II: $M_\infty = 10$, $Kn_\infty = 0.1$ and Altitude $= 75\,km$.

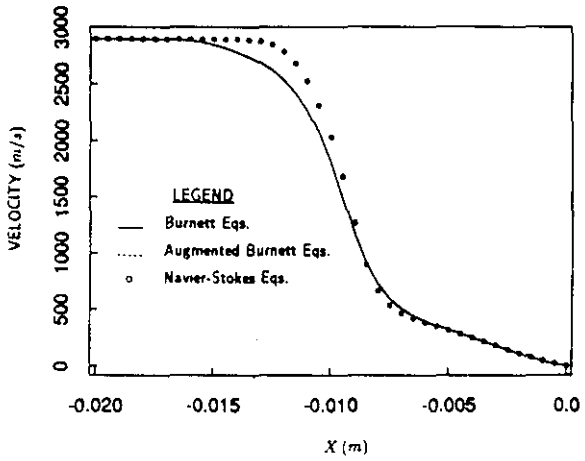

Figure 16: Velocity along stagnation streamline for Case II: $M_\infty = 10$, $Kn_\infty = 0.1$ and Altitude = $75\,km$.

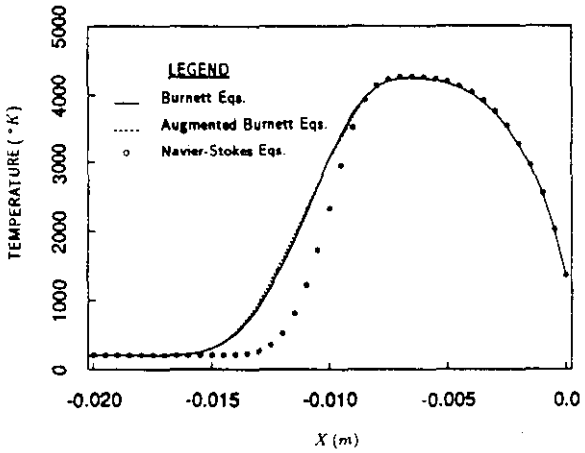

Figure 17: Temperature along stagnation streamline for Case II: $M_\infty = 10$, $Kn_\infty = 0.1$ and Altitude = $75\,km$.

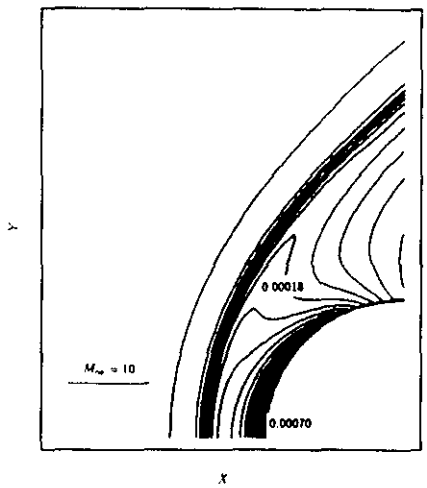

Figure 18: Navier-Stokes density contours for Case II: $M_\infty = 10$, $Kn_\infty = 0.1$ and Altitude = $75\,km$.

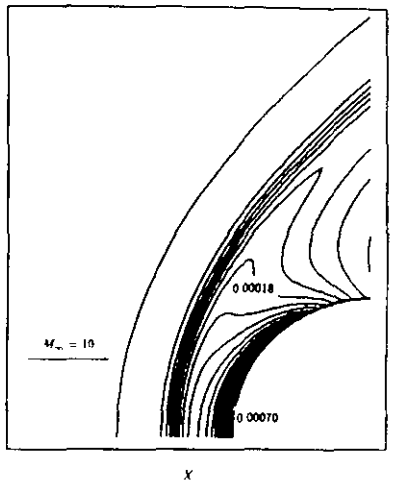

Figure 19: Augmented Burnett density contours for Case II: $M_\infty = 10$, $Kn_\infty = 0.1$ and Altitude = $75\,km$.

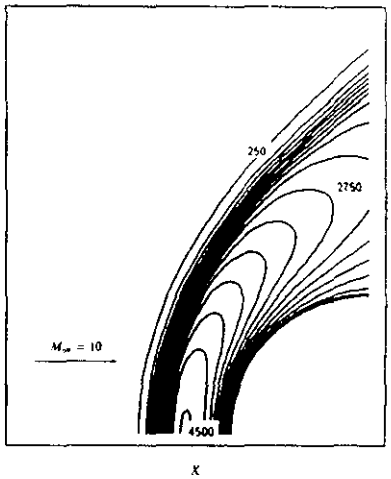

Figure 20: Navier-Stokes temperature contours for Case II: $M_\infty = 10$, $Kn_\infty = 0.1$ and Altitude = $75\,km$.

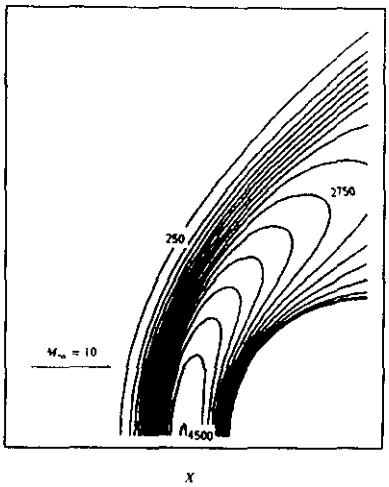

Figure 21: Augmented Burnett temperature contours for Case II: $M_\infty = 10$, $Kn_\infty = 0.1$ and Altitude = $75\,km$.

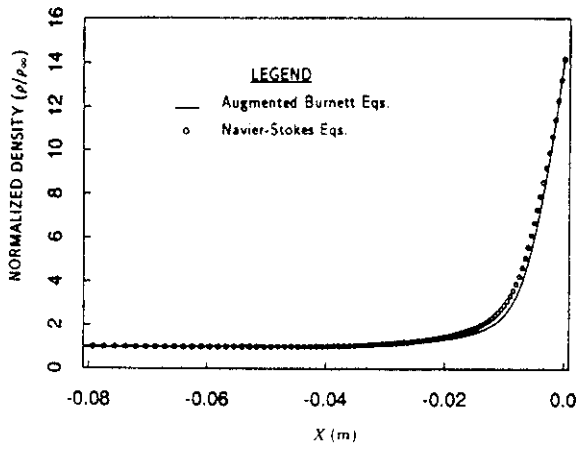

Figure 22: Density along stagnation streamline for Case III: $M_\infty = 10$, $Kn_\infty = 1.2$ and Altitude $= 90\,km$.

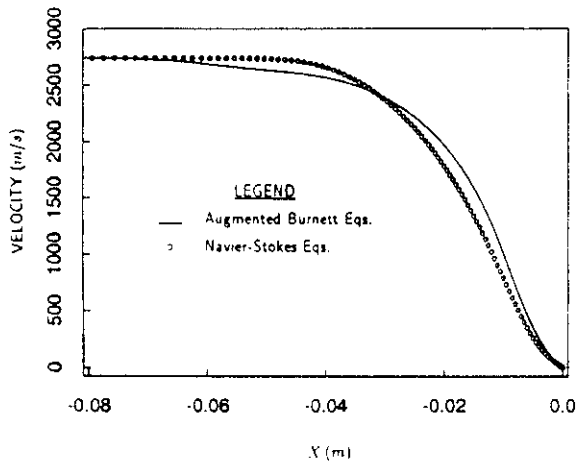

Figure 23: Velocity along stagnation streamline for Case III: $M_\infty = 10$, $Kn_\infty = 1.2$ and Altitude $= 90\,km$.

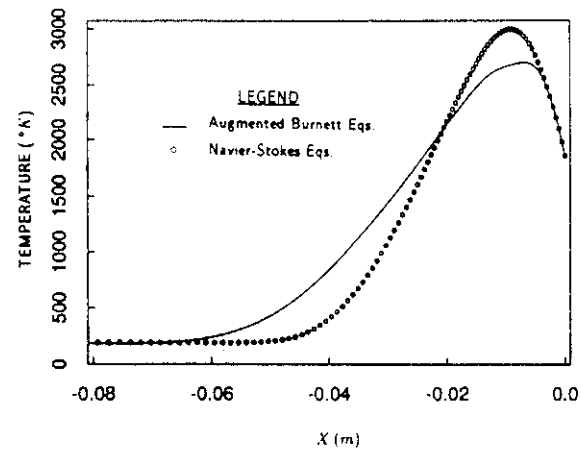

Figure 24: Temperature along stagnation streamline for Case III: $M_\infty = 10$, $Kn_\infty = 1.2$ and Altitude $= 90\,km$.

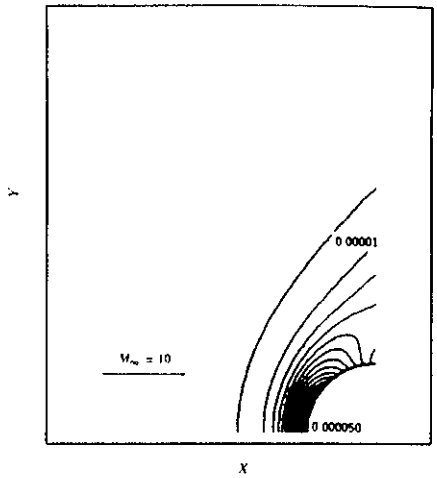

Figure 25: Navier-Stokes density contours for Case III: $M_\infty = 10$, $Kn_\infty = 1.2$ and Altitude $= 90\,km$.

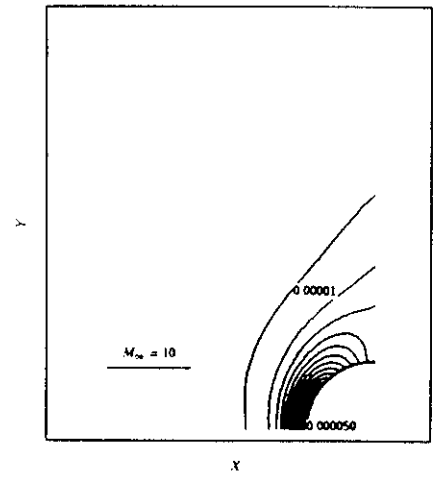

Figure 26: Augmented Burnett density contours for Case III: $M_\infty = 10$, $Kn_\infty = 1.2$ and Altitude $= 90\,km$.

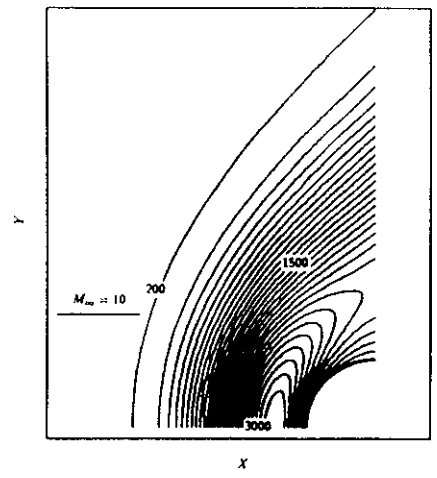

Figure 27: Navier-Stokes temperature contours for Case III: $M_\infty = 10$, $Kn_\infty = 1.2$ and Altitude $= 90\,km$.

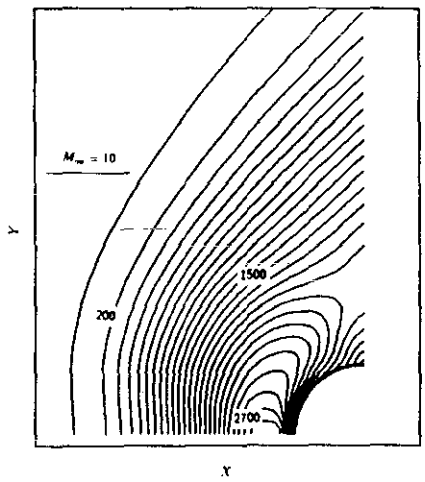

Figure 28: Augmented Burnett temperature contours for Case III: $M_\infty = 10$, $Kn_\infty = 1.2$ and Altitude = $90\,km$.

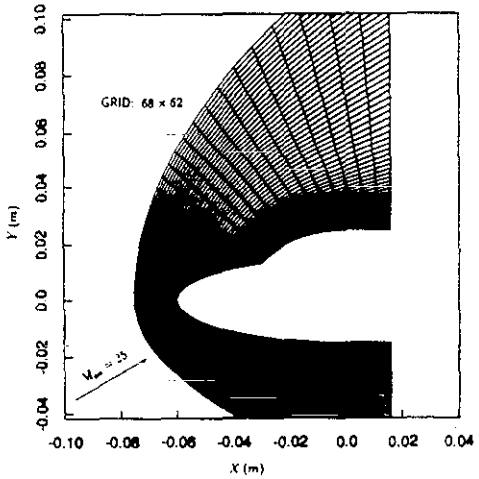

Figure 29: Computational Mesh for Case IV: $M_\infty = 25$, Angle of Attack = 30° and $\lambda_\infty = 1.05 \times 10^{-3}$.

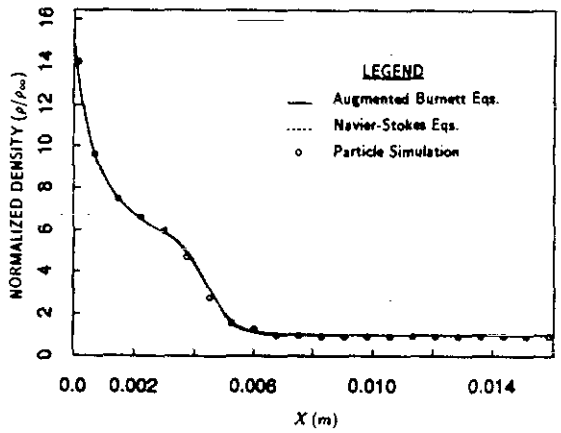

Figure 30: Density along stagnation streamline for Case IV: $M_\infty = 25$, Angle of Attack = 30° and $\lambda_\infty = 1.05 \times 10^{-3}$.

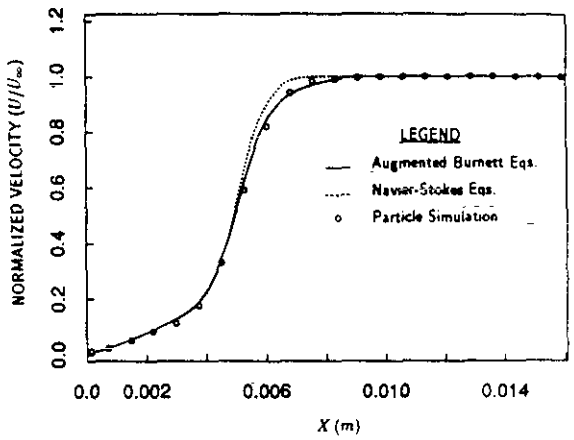

Figure 31: Velocity along stagnation streamline for Case IV: $M_\infty = 25$, Angle of Attack = 30° and $\lambda_\infty = 1.05 \times 10^{-3}$.

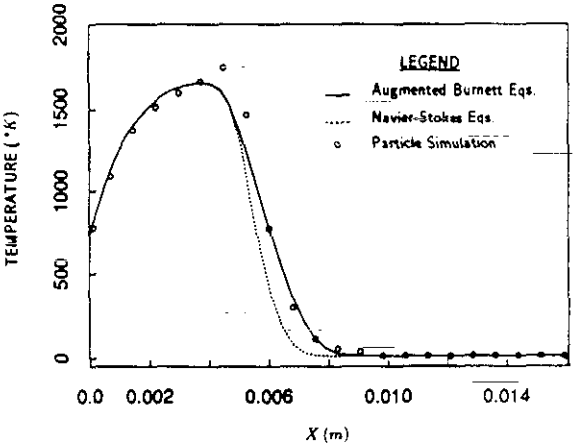

Figure 32: Translational temperature along stagnation streamline for Case IV: $M_\infty = 25$, Angle of Attack = 30° and $\lambda_\infty = 1.05 \times 10^{-3}$.

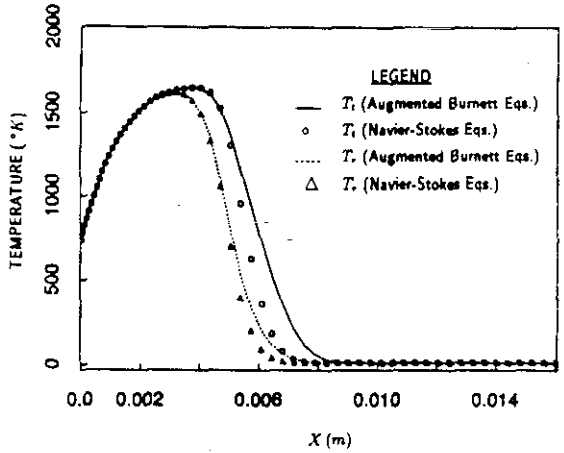

Figure 33: The rotational and translational temperature along stagnation streamline for Case IV: $M_\infty = 25$, Angle of Attack = 30° and $\lambda_\infty = 1.05 \times 10^{-3}$.

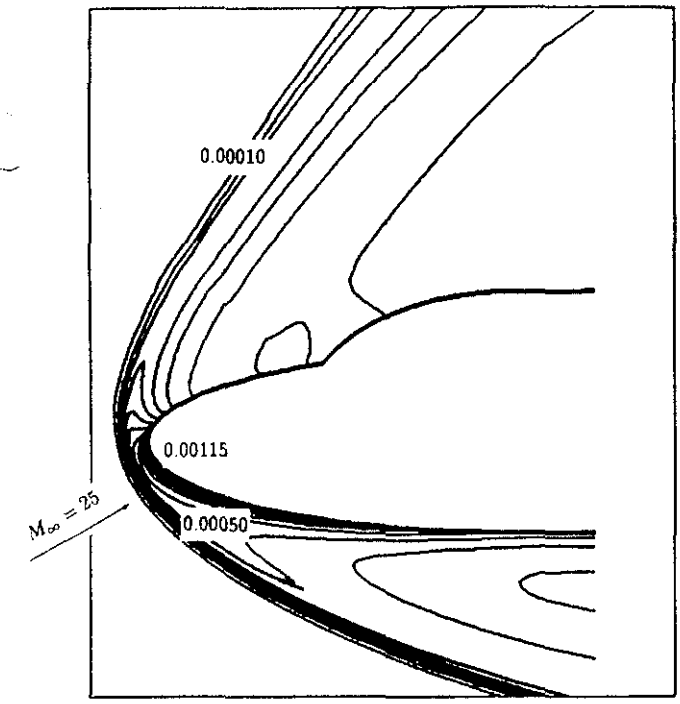

Figure 34: Augmented Burnett density contours for Case IV: $M_\infty = 25$, Angle of Attack = 30 ° and $\lambda_\infty = 1.05 \times 10^{-3}$.

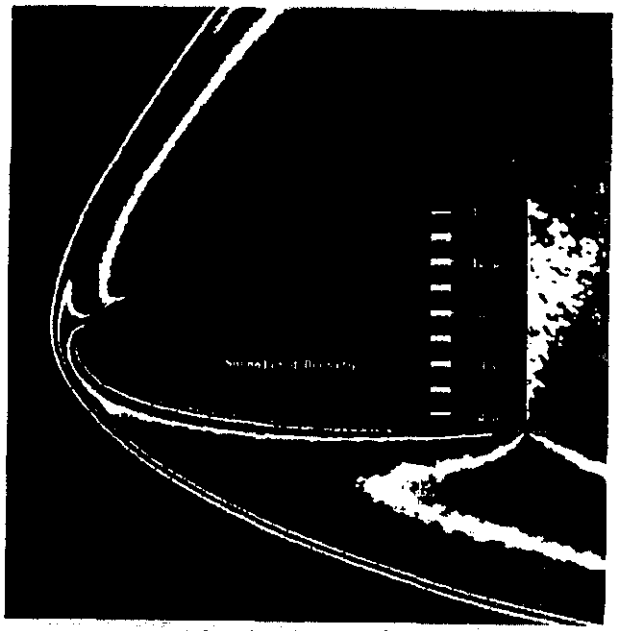

Figure 36: Particle simulation density contours by Feiereisen for Case IV: $M_\infty = 25$, Angle of Attack = 30 ° and $\lambda_\infty = 1.05 \times 10^{-3}$.

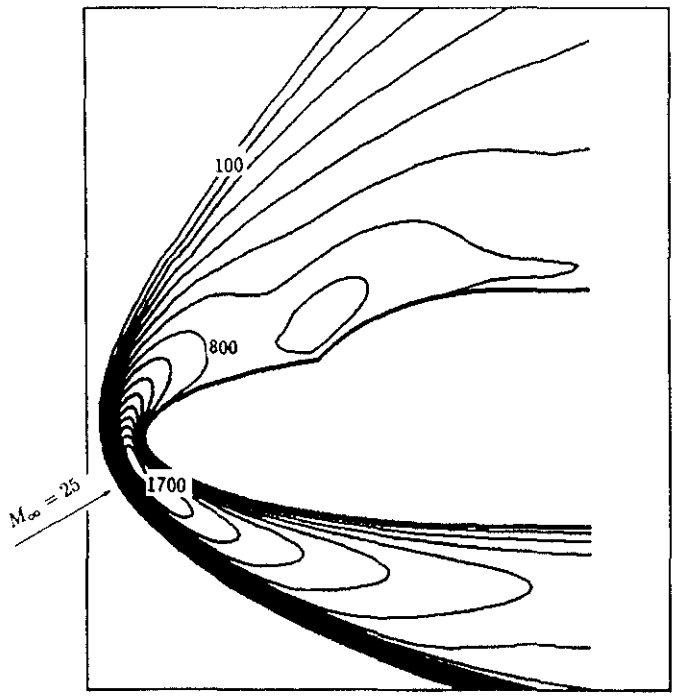

Figure 35: Augmented Burnett translational temperature contours for Case IV: $M_\infty = 25$, Angle of Attack = 30 ° and $\lambda_\infty = 1.05 \times 10^{-3}$.

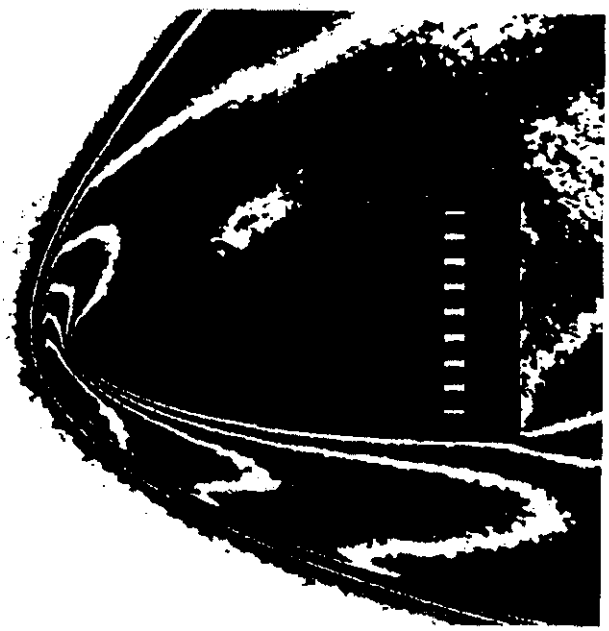

Figure 37: Particle simulation translational temperature contours by Feiereisen for Case IV: $M_\infty = 25$, Angle of Attack = 30 ° and $\lambda_\infty = 1.05 \times 10^{-3}$.